J. Fluid Mech. (1997), *vol.* 341, *pp.* 127–163. Printed in the United Kingdom

Three-dimensionally perturbed vortex tubes in a rotating flow

By G. F. CARNEVALE[1], M. BRISCOLINI[2], R. C. KLOOSTERZIEL[3] AND G. K. VALLIS[4]

[1]Scripps Institution of Oceanography, University of California, San Diego, La Jolla, CA 92093-0225, USA

[2]STSS Technical Center Europe, P. le Giulio Pastore 6, 00144 Roma, Italy

[3]School of Ocean and Earth Science and Technology, University of Hawaii, Honolulu, HI 96822, USA

[4]Department of Ocean Science and Institute of Nonlinear Science, University of California, Santa Cruz, CA 95064, USA

(Received 6 May 1996 and in revised form 21 January 1997)

Numerical experiments are used to study the evolution of perturbed vortex tubes in a rotating environment in order to better understand the process of two-dimensionalization of unsteady rotating flows. We specifically consider non-axisymmetric perturbations to columnar vortices aligned along the axis of rotation. The basic unperturbed vortex is chosen to have a Gaussian cross-sectional vorticity distribution. The experiments cover a parameter space in which both the strength of the initial perturbation and the Rossby number are varied. The Rossby number is defined here as the ratio of the maximum amplitude of vorticity in the Gaussian vorticity profile to twice the ambient rotation rate. For small perturbations and small Rossby numbers, both cyclones and anticyclones behave similarly, relaxing rapidly back toward two-dimensional columnar vortices. For large perturbations and small Rossby numbers, a rapid instability occurs for both cyclones and anticyclones in which antiparallel vorticity is created. The tubes break up and then re-form again into columnar vortices parallel to the rotation axis (i.e. into a quasi-two-dimensional flow) through nonlinear processes. For Rossby numbers greater than 1, even small perturbations result in the complete breakdown of the anticyclonic vortex through centrifugal instability, while cyclones remain stable. For a range of Rossby numbers greater than 1, after the breakdown of the anticyclone, a new weaker anticyclone forms, with a small-scale background vorticity of spectral shape given approximately by the $-5/3$ energy spectral law.

1. Introduction

Ambient rotation can significantly alter the evolution and subsequent properties of three-dimensional turbulence, or indeed of any initially three-dimensional flow. Experiments in rotating tanks and numerical simulations of rotating turbulence show the strong tendency of rotation to two-dimensionalize the flow. This process is sometimes 'explained' by recourse to the Taylor–Proudman theorem, but this important theorem is concerned solely with the steady-state flow, and does not tell us how, or even whether, a flow will evolve toward a two-dimensional state. Linear analysis of inertial waves illuminates one path to two-dimensionality, but this can be

the full explanation only when motions are very slow and nonlinear effects are very weak. Plainly this is not the case in turbulent flows where two-dimensionalization nevertheless remains an important phenomenon. There have been a number of recent articles on this geophysically important process, but it is still not fully understood. Thus, to gain further insight, we have studied the effect of rotation on one simple special case – the vortex column. Specifically, we have performed a series of numerical simulations in which vortex columns aligned along an ambient rotation axis are perturbed by non-axisymmetric, three-dimensional disturbances.

Let us further motivate our work with a few observations and comments on previous numerical and experimental results. In rotating-tank experiments, one readily observes the striking phenomenon of a localized three-dimensional turbulent flow rapidly being transformed into Taylor columns, that is, cylindrical structures with hardly any variation in the direction of the axis of rotation. For example, Flierl, Stern & Whitehead (1983) injected a narrow turbulent jet horizontally into a rotating homogeneous fluid and observed the entire flow to organize itself rapidly into a few nearly perfect Taylor columns. The rotating-tank experiments by Hopfinger, Browand & Gagne (1982) show the generation of two-dimensional vortices from an oscillating grid that creates a local region of three-dimensional turbulence at the bottom of the tank. From the small-scale three-dimensional turbulence, intense cyclones extend, along the rotation axis, far from the generation region. High-resolution numerical simulations have shown that rotation profoundly influences three-dimensional turbulence. Bardina, Ferziger & Rogallo (1985) showed that in simulations of freely decaying turbulence, rotation decreases the rate of decay of the total energy and increases length scales in the direction of the axis of the applied rotation. In 1989, Cambon & Jacquin, using a closure theory, showed that rotation creates a transfer of energy toward towards horizontal wave-vector orientations. These aspects of rotating turbulence were verified in laboratory experiments (Jacquin *et al.* 1990). Cambon, Jacquin & Lubrano (1992) conclude that the tendency toward two-dimensionalization in rotating turbulence at moderate Rossby numbers must somehow be mediated by nonlinear effects. In a turbulent flow, the effects of vortex–vortex interaction are strong, and separating out the effects of rotation is difficult. Therefore, it is useful to study the effects of rotation on a single rapidly evolving vortex.

Just as striking as the two-dimensionalization of turbulent flows in rotating-tank experiments is the violent disruption of strong anticyclones by the presence of background rotation. Kloosterziel & van Heijst (1991) observed instabilities of strong anticyclones that lead to violent turbulent mixing followed by Taylor–Proudman column formation of weak cyclones and anticyclones. It was shown by Kloosterziel & van Heijst (1991), through an extension of Rayleigh's criterion to rotating flows, that anticyclones are only centrifugally stable for sufficiently small Rossby numbers. For large Rossby numbers there is an annular region surrounding the core where the Rayleigh discriminant is negative. Overturning (centrifugal) instabilities are expected to occur, if at all, in this annular region (see §3.2). This is a linear stability criterion which cannot predict what happens as the instability grows to finite amplitude. Nor does it explicitly deal with the question of three-dimensional perturbations, but rather treats the field as azimuthally symmetric. Lesieur, Yanase & Metais (1991) studied the evolution of an array of vortices in a rotating shear flow. One of the questions raised by Lesieur *et al.* (1991) was at what Rossby number would anticyclones be most rapidly destroyed? This has been further examined by Bartello, Metais & Lesieur (1994) and Cambon *et al.* (1994) who demonstrated that, in numerical simulations

of an array of strong vortices of alternating sign, the anticyclones were completely disrupted. In a recent article, Mahalov & Zhou (1996) develop a formalism for rotating turbulence based on EDQNM closure theory that attempts to isolate the effects of rotation.

Smyth & Peltier (1994) studied the influence of rotation on the stability of a single vortex which results from the merger of two vortices that are created during the Kelvin–Helmholtz instability of a parallel shear flow. Contours of vorticity and streamfunction are elliptical in shape in this case. This vortex is quasi-steady while embedded in the surrounding shear flow. They studied the stability of this flow as a function of Rossby number and the wavelength of the perturbation along the (vertical) axis of rotation. A very rapidly growing 'edge mode' was identified which is located in the region surrounding the core of the vortex where the extended Rayleigh criterion suggests that (centrifugal) instability should reside. Their study was essentially a normal modes analysis, and as such can only predict what will happen during the early evolution of their perturbed vortex embedded in a shear flow. They identified the Rossby number and vertical length scale of the perturbation at which the edge mode has the highest growth rate. Here we extend their results by investigating in further detail the destabilization and long-term evolution of single cyclones and anticyclones with a Gaussian vorticity profile subject to rotation in the absence of shear. In these cases the localized vorticity distributions are circularly symmetric about the vertical (rotation) axis. Because of the difference in flow types, the extent to which Smyth & Peltier's (1994) results can meaningfully be compared to ours is not *a priori* obvious. But, as we will see, our findings do roughly correspond to theirs.

The choice of a Gaussian vorticity profile is motivated by previous laboratory experience and stability considerations. In Carnevale, Kloosterziel & van Heijst (1991), Kloosterziel & van Heijst (1991) and Carnevale & Kloosterziel (1994), through rotating-tank experiments, we examined the evolution of vortices with both Gaussian vorticity profiles and zero-circulation profiles (in which an annulus of oppositely signed vorticity surrounds the vortex core). The vortices with zero-circulation profiles undergo two-dimensional instabilities, which, although interesting, are not the object of the present study. In order to focus on three-dimensional processes, we use the Gaussian profile which is nonlinearly stable to purely two-dimensional instabilities (cf. Carnevale & Shepherd 1990; Dritschel 1988).

Note that even for vortex tubes that are centrifugally stable, the tendency toward two-dimensionalization leads us to anticipate another form of vortex breakdown. Consider a centrifugally stable vortex tube perturbed so that its axis deviates from the axis of rotation of the environment. To be specific, consider the z-axis to be the axis of rotation of the environment, and imagine a vortex tube to be perturbed such that it is displaced from the z-axis by an amount $\Delta y = A(1 + \cos \kappa z)$ in the y-direction. The tendency for the different parts of the tube, with maximum but opposite displacements from the z-axis, to align along the ambient rotation axis leads to a breakdown of the vortex column as we discuss in detail below.

The rest of the paper is organized as follows. The first few sections contain preparatory material concerning aspects of the evolution equations (§2), the linear theory (§3) and the initial conditions used for the simulations (§4) that are important for understanding our results. In §5 we briefly describe the numerical methods. In §6 we present the results for small perturbations for vortices with small (§6.1) and large Rossby numbers (§6.2). In §7 we discuss the case of large perturbations, again both for small (§7.1) and large Rossby numbers (§7.2) In §8 a summary and discussion of the main results is given.

2. Evolution equations

Ideally, we wish to consider near-inviscid incompressible homogeneous flow subject to a constant background rotation. We assume the rotation is about the z-axis, that is, the rotation vector is given by $\boldsymbol{\Omega} = \Omega\hat{\boldsymbol{z}}$. Thus the velocity evolution equation is the Euler equation:

$$\frac{\partial \boldsymbol{u}}{\partial t} + \boldsymbol{u}\cdot\nabla\boldsymbol{u} + 2\boldsymbol{\Omega}\times\boldsymbol{u} = -\frac{1}{\rho}\nabla p, \tag{2.1}$$

$$\nabla\cdot\boldsymbol{u} = 0, \tag{2.2}$$

where $\boldsymbol{u}$ is the divergenceless three-dimensional velocity field, ρ the fluid density, assumed constant, and p the pressure field. The Euler equation can be rewritten in a more convenient form as

$$\frac{\partial \boldsymbol{u}}{\partial t} = -\frac{1}{\rho}\nabla(p + \tfrac{1}{2}u^2) + \boldsymbol{u}\times\boldsymbol{\omega}_a, \tag{2.3}$$

where $\boldsymbol{\omega} = \nabla\times\boldsymbol{u}$ is the relative vorticity vector and $\boldsymbol{\omega}_a = \boldsymbol{\omega} + 2\boldsymbol{\Omega}$ is the absolute vorticity vector. By taking the curl of this equation, we readily obtain the equation for the advection of vorticity in three dimensions:

$$\frac{\partial \boldsymbol{\omega}_a}{\partial t} = \nabla\times(\boldsymbol{u}\times\boldsymbol{\omega}_a) = \nabla\times(\boldsymbol{u}\times\boldsymbol{\omega} + \boldsymbol{u}\times 2\boldsymbol{\Omega}). \tag{2.4}$$

This last equation has the same form as in the case without rotation, except that here the advected quantity is the absolute rather than the relative vorticity. Thus Kelvin's circulation theorem still applies except in terms of the absolute (or potential) vorticity and absolute circulation. Thus absolute vortex elements are material. Also since $\nabla\cdot\boldsymbol{\omega}_a = 0$, the flux through absolute vorticity tubes is invariant along the tube.

To these evolution equations we must append boundary conditions. Seeking the simplest situation in which to examine the effects of rotation, we use triply periodic boundary conditions, thus avoiding the formation of boundary layers. If we use a Fourier spectral representation of the fields, the inversion formula for the velocity is simply given by

$$\boldsymbol{u}_{\boldsymbol{k}} = \mathrm{i}\frac{\boldsymbol{k}\times\boldsymbol{\omega}_{\boldsymbol{k}}}{k^2}, \tag{2.5}$$

where, $\boldsymbol{u}_{\boldsymbol{k}}$ and $\boldsymbol{\omega}_{\boldsymbol{k}}$ are the Fourier amplitudes of the velocity and vorticity fields for wave vector $\boldsymbol{k}$, respectively, and $k = |\boldsymbol{k}|$. Note that $\boldsymbol{u}_{\boldsymbol{k}}$ and $\boldsymbol{\omega}_{\boldsymbol{k}}$ are three-dimensional vectors.

3. Linear theory

In this section we briefly review the linear dynamics for a rotating homogeneous fluid. Small perturbations in an otherwise quiescent rotating fluid will disperse as inertial waves (sometimes called gyroscopic waves). However, if a steady vortex tube is present, linearization of the dynamics about this vortex is needed to investigate what happens at early times when it is exposed to small perturbations. Normal modes analysis restricted to the case of axisymmetric perturbations leads to a criterion for centrifugal stability (sufficient for linear stability and necessary for linear instability) which has been found to be a useful guideline regarding the question of stability to more general perturbations.

3.1. *Inertial waves*

The dynamics of inertial waves is obtained by linearization about the state of no motion. In other words we will linearize the dynamics by dropping the advective term in (2.1) or, equivalently, by dropping the $\boldsymbol{u} \times \boldsymbol{\omega}$ term in (2.4) to obtain

$$\frac{\partial \boldsymbol{\omega}}{\partial t} = 2\Omega \nabla \times (\boldsymbol{u} \times \hat{\boldsymbol{z}}). \tag{3.1}$$

Then, if we Fourier transform and use the diagnostic relation (2.5), we obtain

$$\dot{\boldsymbol{\omega}}_{\boldsymbol{k}} = \frac{2\Omega}{k^2} \boldsymbol{k} \times (\hat{\boldsymbol{z}} \times (\boldsymbol{k} \times \boldsymbol{\omega}_{\boldsymbol{k}})) = -\frac{2\Omega k_z}{k^2} \boldsymbol{k} \times \boldsymbol{\omega}_{\boldsymbol{k}}, \tag{3.2}$$

where a dot denotes the time-derivative and where k_z is the z-component of the vector $\boldsymbol{k} = \hat{\boldsymbol{x}} k_x + \hat{\boldsymbol{y}} k_y + \hat{\boldsymbol{z}} k_z$. This can be written in matrix notation as

$$\dot{\boldsymbol{\omega}}_{\boldsymbol{k}} = \frac{2\Omega k_z}{k^2} \begin{bmatrix} 0 & k_z & -k_y \\ -k_z & 0 & k_x \\ k_y & -k_x & 0 \end{bmatrix} \boldsymbol{\omega}_{\boldsymbol{k}}. \tag{3.3}$$

If we decompose the temporal evolution into the Fourier modes, $e^{i\alpha t}$, we find by taking the time derivative of (3.2) the dispersion relation

$$\alpha^2 = (2\Omega)^2 k_z^2 / k^2 = (2\Omega)^2 (\sin\theta)^2, \tag{3.4}$$

where θ is the angle between the wave vector $\boldsymbol{k}$ and the horizontal plane (the axis of rotation is assumed to be along the vertical). This is a continuous spectrum where the magnitude of the frequency takes values anywhere from 0 to 2Ω. Energy propagates with the group velocity given by

$$\boldsymbol{c}_g = \frac{2\Omega}{k^3} (-k_x k_z, -k_x k_z, k_x^2 + k_y^2), \tag{3.5}$$

which is is perpendicular to the wavevector and has a magnitude

$$|\boldsymbol{c}_g| = \frac{2\Omega}{|\boldsymbol{k}|} |\cos\theta|. \tag{3.6}$$

In particular, for any given wavenumber, the group velocity is maximal for $\theta = 0$, i.e. for horizontal wavevectors with group velocity aligned along the z-axis. According to (3.4), these are the zero-frequency waves. Taylor-column formation, as observed when an object is slowly towed through a rotating fluid, can be explained as being due to the vertical propagation of all the zero-frequency waves with group velocities higher than the horizontal speed of the object (Greenspan 1968; Lighthill 1978). In the linear dynamics, the zero-frequency waves, which have $k_z = 0$, are the Fourier modes for the Taylor column, the geostrophically balanced part of the flow (u, v depth and time independent and w zero everywhere). For all other k_z the wavevectors are not purely horizontal and will thus propagate away in a direction which has a non-zero angle from the vertical, with frequencies somewhere between 0 and 2Ω.

Under the linear dynamics, the free inertial waves will evolve independently, each oscillating with the appropriate frequency. In a sufficiently large domain, we will see linear radiation away from the initially confined region of vorticity. All modes will evolve except the zero-frequency modes. This will tend to leave a vortex with no z-dependence. In the finite and periodic domain, the radiation leaving in one direction re-enters the domain from the opposite direction and eventually perturbs the vortex again. Since there are many different frequencies of oscillation represented by the

inertial modes, the interference is not constructive and one does not soon return to the initial state.

3.2. *Centrifugal instability*

To better understand the behaviour of individual vortex tubes in a rotating system, we will look at the role of centrifugal instabilities. In particular, we consider the case of a vortex tube whose axis is parallel to the rotation axis (z-axis), with a depth-independent flow field (Taylor column). The simplest case is that of a circularly symmetric flow. In cylindrical polar coordinates (r, θ, z) the velocity field has only an azimuthal component u_θ (swirling flow), and only the vertical component of the vorticity, ω_z, is non-zero. For such a flow, the Rayleigh criterion for centrifugal instability is that the magnitude of the angular momentum of the flow must somewhere be a decreasing function of the distance from the axis of rotation. To obtain this criterion, Rayleigh (1916) invoked an energy argument in which two concentric fluid rings were imagined to be interchanged while conserving their angular momentum. This argument also points out that the instability can only occur in the annular region where the magnitude of the angular momentum decreases with radius. Including the background rotation, this criterion means that there can be instability if for some range of r we have (Kloosterziel & van Heijst 1991)

$$(\Omega r + u_\theta)(2\Omega + \omega_z) < 0, \tag{3.7}$$

where Ω is the ambient rotation rate, and r is the radial distance from the centre of the vortex axis. The range of r-values for which (3.7) is true can be considered to define a region of (possible) instability. Although, strictly speaking, the Rayleigh criterion applies only to axisymmetric perturbations, we have found it a useful guide also to the stability of the Gaussian vortex tube subjected to three dimensional perturbations, as will be seen below. Smyth & Peltier (1994) arrived at the same conclusion in their study of an elliptically shaped vortex tube embedded in a shear flow in a rotating system.

We will consider a Gaussian vorticity profile

$$\omega_z = \omega_0 \exp\left(-r^2/2\sigma^2\right). \tag{3.8}$$

Substituting this ω_z into the criterion (3.7), we see that there can be instability only if the vortex is an anticyclone. Furthermore, for instability, the anticyclone must satisfy somewhere the criterion

$$(1 - (Ro/\mu)(1 - \mathrm{e}^{-\mu}))(1 - Ro\,\mathrm{e}^{-\mu}) < 0, \tag{3.9}$$

where $\mu = r^2/(2\sigma^2)$, and where we have defined the Rossby number by $Ro = |\omega_0/2\Omega|$.

Figure 1 shows plots of the left-hand side of (3.9) for values of Ro near 1. For Ro less than 1, this criterion is nowhere satisfied and thus the anticyclone is centrifugally stable, while for $Ro > 1$ there will always be a region in which the instability criterion is satisfied. To see this, first note that if $Ro < 1$ then $1 - Ro\,\mathrm{e}^{-\mu} > 0$. Thus the sign of the left-hand side of (3.9) will be the same as the sign of $h(\mu) \equiv (1 - (Ro/\mu)(1 - \mathrm{e}^{-\mu}))$. Since $0 \leqslant (1 - \mathrm{e}^{-\mu})/\mu \leqslant 1$, we have $h(\mu) \geqslant 1 - Ro > 0$, and so the stability criterion is satisfied for all $Ro < 1$. For $Ro > 1$ there is always an annulus in which the stability criterion is not satisfied. The inner radius of this annulus is given by $\mu = \ln Ro$. Thus the distance of this annulus from the centre of the vortex increases as Ro increases. The outer boundary of the annulus is given approximately by $\mu = 2(Ro - 1)/Ro$ for $Ro \approx 1$ and by $\mu \sim Ro$ for Ro large.

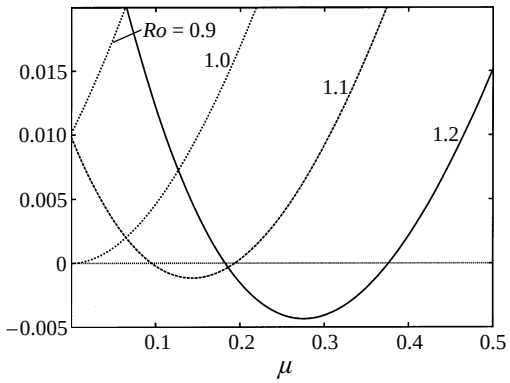

FIGURE 1. The left-hand side of equation (3.9) versus $\mu = r^2/(2\sigma^2)$, for the case of an anticyclone.

For Ro near the stability critical value $Ro = 1$, the inner radius of the annulus is given by $r_1 = \sigma[2(Ro-1)]^{1/2}$ and the outer radius by $r_2 = 2\sigma[(Ro-1)/Ro]^{1/2}$. Thus, for $Ro \gtrsim 1$ the region of instability is deep within the core of the vortex. In this case, the instability must rapidly involve the entire core of the vortex. For large Ro, the inner radius of the annulus is given by $r_1 = \sigma(2\ln Ro)^{1/2}$ and the outer radius by $r_2 = \sigma(2Ro)^{1/2}$. Thus, for sufficiently large Ro, the instability will begin far from the vortex core. In the limit of $Ro \to \infty$, the cyclone and anticyclone must become indistinguishable. In addition, the Rayleigh criterion shows that without background rotation the Gaussian vortex is centrifugally stable. The recovery of this stability in the case of the anticyclone is seen here in the way that the inner radius of the region of instability moves out to $r \to \infty$ as $Ro \to \infty$.

The centrifugal instability criterion is based on the supposition that the disturbances remain axisymmetric. Normal modes analysis (linear stability analysis) of the stability of vortex tubes in a non-rotating environment started with a paper by Lord Kelvin (1880). An axisymmetric normal mode, in cylindrical polar coordinates (r, θ, z), is proportional to $\exp(\mathrm{i}(k_z z - \alpha t))$ with a prefactor dependent on r but not on θ. Such modes will periodically pinch and bulge the vortex core, and they are therefore sometimes called 'sausage' modes. Such modes can travel on a vortex tube without causing vortex breakdown if the tube is centrifugally stable (α real). Although the Rayleigh criterion (3.7) was arrived at by pure mechanistic arguments, it can also be arrived at by performing a normal modes analysis similar to Chandrasekhar's (1961) treatment of the question of stability of Couette flow. Negative values of the Rayleigh discriminant are then found to be a necessary condition for linear instability with respect to axisymmetric normal mode perturbations of the above form. For an example of these modes (on a Rankine vortex) in a non-rotating system see Saffman (1992). Rayleigh's criterion for vortex tubes in a stratified fluid has recently been investigated by Miyazaki & Fukomoto (1991). As in a non-stratified fluid they found that the vortex tube acts as a waveguide for axisymmetric waves, which have in their case frequencies above the (constant) buoyancy frequency of the environment. We are, however, not aware of similar theoretical studies where the vortex is embedded in a rotating environment. In a series of experiments which were initiated with axisymmetric perturbations, we did observe the evolution of sausage modes even with strong background rotation. In the present paper we will not consider axisymmetric perturbations; however, as we will see below, in some cases our perturbed vortex tubes will show signs of the 'sausage modes.'

Another important mode of oscillation of the vortex tube in a non-rotating environment is the 'bending' mode, which has a structure proportional to $\exp\{\mathrm{i}(k_z z + m\theta - \alpha t)\}$, with $m = 1$ and with a prefactor which is a function of r. In this case the axis of the tube is periodically bent in the vertical. In fact, an initially straight vortex tube when subjected to a 'bending'-type normal mode is deformed into a spiralling, helical tube. Again, we are not aware of any theoretical studies where the dispersion relation and radial structure of stable bending modes have been determined for the Gaussian vortex tube in a rotating environment.

We mention finally that straight vortex tubes with uniform vorticity are stable to both the 'sausage' and the 'bending' type of perturbations (Saffman 1992). However, when axial flow is present, such a vortex tube can be unstable to the bending mode perturbation (Lundgren & Ashurst 1989). When the uniform vortex tube is embedded in an external straining field, it is unstable within a range of vertical wavenumbers k_z to the bending mode perturbations. The vortex tube is then the Moore–Saffman elliptical vortex (Saffman 1992). To sum up, in a non-rotating environment the circular tube is linearly stable, but unstable in a shear flow. Thus, it is not obvious how much of the information contained in Smyth & Peltier's (1994) paper regarding the stability of an elliptical vortex in a shear flow in a rotating system can be meaningfully compared with the results for circular vortex tubes in a quiescent rotating environment.

4. Initial three-dimensional perturbation

As discussed above, the basic unperturbed state in this study is the vortex tube with Gaussian vorticity profile. In the series of simulations that we will discuss, the initial Rossby number of the vortex is varied while the thickness of the vortex is held fixed. It was desirable to choose the width of the vortex to be small in order to minimize the interference between the evolution of the vortex and its periodic images. Simultaneously, adequate resolution of the core of the vortex required that the radius of the core be not too small. In units in which the computational domain is taken to be the triply periodic box of side $L = 2\pi$, a reasonable choice was found to be $\sigma = 0.25$. Since our primary purpose here is to consider the asymmetries due to the effects of rotation alone, we have used the same domain size and the same resolution in each direction to avoid introducing asymmetries in the computational scheme. Thus, the ratio σ/L of the horizontal vortex length scale to the vertical scale of the computational domain is about 0.04. In the laboratory experiments of Carnevale *et al.* (1991), this aspect ratio was about 0.1, while in the experiments of Hopfinger *et al.* (1982) it was about 0.01. Therefore, our choice gives a ratio that is intermediate between that found in these two sets of experiments. Our results should be representative of the effects of rotation in a variety of situations typical of recent laboratory investigations. On the other hand, detailed comparisons with specific laboratory experiments would require attention to effects such as Ekman boundary layers, which can play an important role, but which are additional and separate complications beyond the scope of this study.

The perturbed vorticity field must, of course, be divergenceless. One convenient method of producing the perturbed state is to take the Gaussian tube and advect it passively and smoothly with a stationary divergenceless velocity field, $\boldsymbol{v}$, for a finite period of time, t. The 'externally imposed' advecting velocity field is then turned off and the resulting vorticity field $\boldsymbol{\omega}$ is taken as the initial condition for our experiment. If $\boldsymbol{v}$ is sufficiently simple, the initial vorticity field can be calculated analytically. If an incompressible velocity field acts on the vector field $\boldsymbol{\omega}(\boldsymbol{x})$ and is such that the material

points originally at $\boldsymbol{a}$ are transported to $\boldsymbol{x}$ at time t, then the advected field is given by (see Batchelor 1967, p. 276)

$$\omega_i(\boldsymbol{x}, t) = \sum_j \frac{\partial x_i}{\partial a_j} \omega_j(\boldsymbol{a}, 0). \tag{4.1}$$

For this formula to be valid, the velocity field which advected the point $\boldsymbol{a}$ to the point $\boldsymbol{x}$ can be arbitrary, save for being incompressible. We take $\boldsymbol{v}$ to be in a direction perpendicular to the original tube axis, constant from time 0 to time t and with spatial variation only along the rotation axis, e.g. $\boldsymbol{v} = (0, v(z_0), 0)$. Thus we have

$$\boldsymbol{\omega}(\boldsymbol{x}, t) = \begin{bmatrix} 0 \\ tv'(z)\omega_0 \exp\{-(x^2 + (y - v(z)t)^2)/2\sigma^2\} \\ \omega_0 \exp\{-(x^2 + (y - v(z)t)^2)/2\sigma^2\} \end{bmatrix}. \tag{4.2}$$

It can be readily checked that $\nabla \cdot \boldsymbol{\omega} = 0$. In the experiments to be presented here, we have chosen to set $v(z) = v_f(1 + \cos \kappa z)$ with v_f fixed. The size of the perturbation then is simply measured by the length of time that the steady advection is applied; call this forcing period t_f. A non-dimensional measure of the size of the perturbation is the maximum distance that the tube axis is moved from the unperturbed position relative to the horizontal size of the tube, σ. This non-dimensional distance is given by $y_f = t_f v_f / \sigma$. We will consider two sizes for the perturbation: one represents a weak tube distortion with $y_f = 0.8$ and the other a strong perturbation with $y_f = 8.0$.

The other parameter to consider is the perturbation wavenumber, κ. In most of the simulations considered here, we have taken $\kappa = 1$, which corresponds to the largest possible wavelength in the z-direction and would be representative of perturbations on the scale of the depth of the fluid in the laboratory experiments. In their linear stability study of the elliptical anticyclone in a shear flow, Smyth & Peltier (1994) showed how the growth rate of the most unstable 'edge mode' varies with the Rossby number and the vertical wavenumber (see their figure 13*b*). In their notation, the vertical wavenumber was denoted by d and maximum growth was found for $d = 2$ and $Ro = 3.3$. The vertical non-dimensional wavelength is $2\pi/d$. Judging from their figure 10(*a*), the major axis of the elliptical vortex is about 15 while the minor axis is about 10 for the contour which indicates the approximate 10% level of the peak vorticity. Thus, the ratio of the horizontal scale of the vortex to the vertical scale of the perturbation lies between $(10/2\pi)d$ and $(15/2\pi)d$. For $d = 2$ the average of this ratio is about 4, so the most unstable mode has a vertical scale four times smaller than the horizontal scale. For our Gaussian vortex the 10% contour of the axisymmetric vorticity distribution occurs at a radius of approximately $r = 2.2\sigma$. In all simulations we used $\sigma = 0.25$. Then the ratio the length scale of a perturbation with vertical wavenumber k_z to the horizontal length scale would be $(1.1/2\pi)k_z$. The maximum growth rate would then be expected to be for wavenumber of $k_z \approx 20$, based on the results of Smyth & Peltier for the elliptical vortex. Although our initial perturbation has a length scale somewhat larger than the wavelength for which we expect maximum growth, we will nevertheless see that this perturbation leads to growth of energy in the small scales during the centrifugal instability of the anticyclonic vortex. We have performed simulations with wavenumbers up to $\kappa = 4$ which corresponds roughly to values of d between 0.1 and 0.4. Judging from Smyth & Peltier's figure 13(*b*) one might expect growth rates to increase monotonically with κ, but for each κ in this range no well-defined maximum occurs as the Rossby number varies. In other words, if we use Smyth & Peltier's (1994) results as a guideline, in this range of

κ, for each κ the growth rate is almost constant as Ro varies upwards from about $Ro = 2$. Smyth & Peltier did not discuss how the structure of the associated edge mode varies with vertical wavenumber. In our simulations we have found very few qualitative differences in the early evolution of the perturbed vortex tubes as κ was doubled from 1 to 2, while adjusting the perturbation amplitude such that the ratio of horizontal deviation from the z-axis and the vertical length scale of the perturbation was constant. In most of the simulations to be discussed below, we use a vertical wavenumber $\kappa = 1$, which allows us to simulate the widest range of length scales that appear to be relevant.

One final point about the initial perturbation concerns its horizontal structure. If the amplitude of the perturbation is very small, that is if $y_f \ll 1$, then, in a cylindrical coordinate representation, the perturbation would be dominated by an azimuthal mode-1 component. For finite values of y_f all azimuthal modes are excited to some extent. Even with the smaller of the two values of y_f that we have used, the mode-2 component of the perturbation is of the same order of magnitude as the mode-1 component. Smyth & Peltier point out that azimuthal mode-1 disturbances are associated with core modes while azimuthal mode-2 instabilities are associated with 'edge modes'. In our studies we have initially excited both of these azimuthal modes.

5. Numerical methods

The numerical simulation scheme that we use is based on the evolution equation (2.3). The code is a pseudo-spectral code de-aliased by the method of Patterson & Orszag (1971) (see Briscolini & Santangelo 1992 for further details). The time-stepping algorithm used to advance the vorticity field is a second-order leap-frog scheme. The Coriolis term in equation (2.3) is simply added to the nonlinear terms in the time-stepping routine. Although we are primarily concerned with inviscid effects, for long-term integrations we must use some form of subgrid-scale modelling to avoid the accumulation of energy at the highest wavenumber. To handle the small-scale motions near the grid-spacing scale, we have used the Kraichnan eddy-viscosity model (Kraichnan 1976; Chollet & Lesieur 1981; Lesieur & Rogallo 1989). In the Fourier transform space, this corresponds to the addition of a dissipation governed by

$$\left(\partial \boldsymbol{u}/\partial t\right)_{diss.} = -\nu(k|k_c)k^2\boldsymbol{u}, \tag{5.1}$$

with

$$\nu(k|k_c) = (0.15 + 5\exp(-3.03k_c/k))\nu(k_c), \tag{5.2}$$

where k_c is spectral cutoff, $\nu(k_c) = (\tau_c k_c^2)^{-1}$ is the viscosity based on the eddy turnover time, that is, $\tau_c = \tau_e(k_c)$ where $\tau_e(k) = (E(k)k^3)^{1/2}$, and $E(k)$ is the isotropic energy spectrum (i.e. the three-dimensional energy spectrum integrated over both polar and azimuthal angles).

We have made comparisons between simulations using Kraichnan eddy viscosity and hyperviscosity. The results for the kind of simulations considered here seem insensitive to the exact choice small-scale dissipation, and we have used the Kraichnan eddy viscosity in all of the runs illustrated here. The spatial resolution of these runs in most cases corresponds to a grid of 64^3 points, although some key runs were performed at resolution 128^3.

We can gain some insight into the role played by nonlinear effects in the two-dimensionalization process by comparing the fully nonlinear evolution with the linear

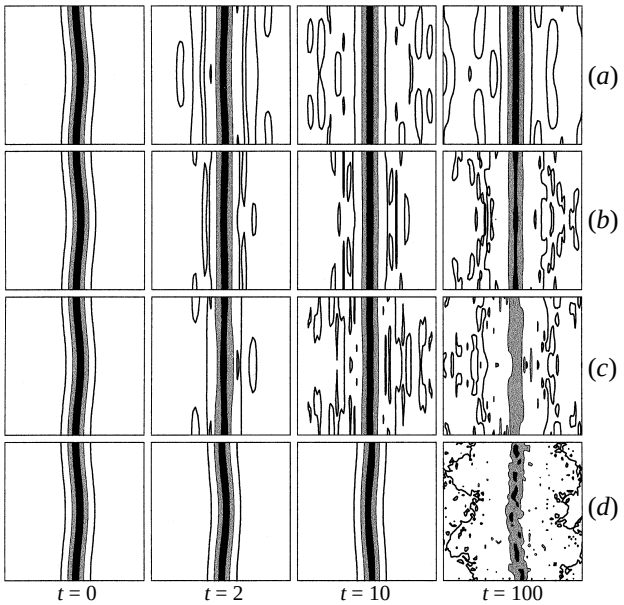

FIGURE 2. Shaded contours of $|\omega|$ in a two-dimensional (y, z)-cross-section of the flow showing the evolution of the vortex with a small three-dimensional perturbation in four different situations: (*a*) according to the purely linear dynamics; (*b*) and (*c*) the results for $Ro = 0.5$ for the cyclone and anticyclone, respectively; (*d*) when $\Omega = 0$. The contour levels represented are (0.025, 0.4 and 0.8) ω_0, with the grey (black) areas having values above 0.4 (0.8) ω_0. The times are in units of $T_\Omega = 2\pi/\Omega$ (which is equal to T_e for $Ro = 0.5$) in (*a–c*). For (*d*) (where $\Omega = 0$) time is measured in units of the eddy turnover time $T_e = 2\pi/|\omega_0|$. In all cases the spatial resolution was 64^3.

dynamics model. To compare the linear evolution with the nonlinear, we incorporate the Kraichnan eddy viscosity in the linear dynamics as well, that is we add (5.1) to (2.1) while dropping the advective term $\boldsymbol{u} \cdot \nabla \boldsymbol{u}$. Thus in comparing the fully nonlinear dynamics with the linear, the only difference will come from the nonlinear advection component.

6. Small perturbations

In this section, we consider the evolution of the vortex tube subject to a weak initial three-dimensional perturbation. We take $y_f = 0.8$ as discussed in the previous section so that the perturbed tube axis direction is nowhere far from the axis of ambient rotation. We will consider the evolution of the initial weakly perturbed column for various Rossby numbers.

6.1. *Small Rossby number*

Taylor–Proudman theory suggests that for very small Rossby number, cyclones and anticyclones will behave very similarly. For example, at $Ro = 0.1$ for the small initial perturbation, we found no significant differences in their behaviour, which essentially was a smooth relaxation toward the unperturbed column. We consider the case of $Ro = 0.5$ as a representative case where the Rossby number is large enough to lead to significant differences between cyclones and anticyclones and yet still small enough to avoid centrifugal instability for the anticyclone. This will also be compared to the case of the vortex tube evolving under purely linear dynamics. Time is measured in

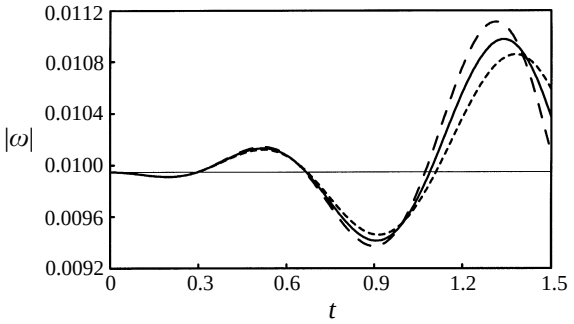

FIGURE 3. Vorticity magnitude versus time at a point $(x, y, z) = (-\pi, 0, 0)$ in the far field during the evolution of the weakly perturbed vortex. Four cases are shown: thick solid curve, linear evolution; long-dashed curve, $Ro = 0.5$ cyclone; short-dashed curve, $Ro = 0.5$ anticyclone; thin solid curve, no ambient rotation. Time is given in units of $T_\omega = 2\pi/\omega$, which, except for the case with no rotation, is the same as T_Ω. $|\omega|$ is in units of $|\omega_0|$.

units of the period of revolution T_Ω of the system, with $T_\Omega = 2\pi/\Omega$. Finally we compare these simulations with the $\Omega = 0$ ($Ro = \infty$) case. If we define an eddy time scale as $T_e = 2\pi/\omega_0$, then for $Ro = 0.5$ we have $T_\Omega = T_e$. Since the vortex columns in these simulations do not deviate far from the initial nearly axial configuration, it is convenient to illustrate the results of the simulations by showing the cross-sectional vorticity distribution in the (y, z)-plane. In figure 2, we show shaded contour plots of the magnitude of the vorticity field in simulations at resolution 64^3. The two higher contour levels are set at $0.4\omega_0$ and $0.8\omega_0$ to give a good indication of the deformations of the core of the vortex during the simulation. The lowest contour level shown is taken at $0.025\omega_0$ to illustrate the weak inertial wave radiation away from the vortex core.

If we consider purely linear evolution, as described above, and if the domain size is large enough, we would expect to see inertial wave radiation from the tube accompanied by a relaxation of the tube toward a structure independent of z, because the only structures which do not change under the linear dynamics are those independent of z. Figure 2(a) confirms this picture. For linear evolution, the magnitude of Ro is immaterial, as long as it is finite, except in setting the time scale for evolution. By time $t = 2T_\Omega$, there has been a good deal of relaxation to two-dimensionality, but the process is not complete. By $t = 10T_\Omega$, the main column is nearly two-dimensional. The variations in the low-level vorticity contours outside the tube in figure 2(a) are due to inertial wave radiation. This background radiation will continue to interact with the main column, so in this periodic domain relaxation cannot ideally be complete, and, in the inviscid case, there is always the possibility, in accordance with the Poincaré recurrence theorem, of the inertial waves on some long time interval interfering constructively again to make a perturbation as strong as in the initial condition, but for the length of this simulation (up to $t = 200T_\Omega$) the profile remained essentially as shown here at $t = 100T_\Omega$.

The early evolution, at least up to time $t = 10T_\Omega$, of the $Ro = 0.5$ cyclone and anticyclone (figure 2b, c) shows essentially the same behaviour as in the linear dynamics case. During this period it appears that linear inertial wave radiation plays the dominant role in the evolution, while in the same period, in the case $Ro = \infty$ (figure 2d), where no radiation is possible, there is no relaxation of the bend in the tube. Note that in the field far from the vortex, the vorticity amplitudes remain low. The contour level value of $0.025\omega_0$ suggests a far-field local Rossby number of

$Ro = 0.025$ for the cyclone and anticyclone. Thus, in that region, the dynamics is to a high degree of accuracy governed by the linear dynamics. In figure 3, we show the magnitude of the vorticity at a test point on the x-axis at a maximum distance from the vortex, during the very early evolution. The concept of group velocity is not strictly applicable here due to the discrete nature of the spatial Fourier spectrum, but keeping that in mind, we can still use the group velocity formula (3.5) to make a rough analysis of figure 3. All of the components of the initial perturbation have $k_z = 1$ (in units in which L, the length of the computational domain, is 2π). The wavevectors in our discrete system that have the highest group velocity and propagate toward our test point have $|k_x| = 1$. Thus, referring to formulas (3.4) and (3.6), we have $\theta = 45°$, and the corresponding wave period is $T_\Omega/\sqrt{2}$. In calculating the arrival time at the test point, it is not clear how to define the distance given the continuous nature of the vorticity distribution. Along the direction $\theta = 45°$, the propagation distance from the tube is at most $L/\sqrt{2}$ (this neglects the thickness of the tube). The formula for the group velocity at this angle then suggests an arrival time of something less than $T_\Omega/\sqrt{2}$. These predictions are roughly in accord with the results shown in figure 3. There is a close correspondence between the signal in the linear dynamics case and the $Ro = 0.5$ cyclone and anticyclone as the wave arrives. There are, however, some differences in phase and amplitude that become significant by time T_Ω. Since the amplitude of the signal suggests that the propagation in the far field is linear, these differences are probably due to the nonlinear interactions in the vortex that change the phase relationships between various components of the inertial wave field. The signal in the $Ro = \infty$ case is also shown in figure 3, but that is essentially constant due to the lack of inertial wave propagation.

Although the early evolution of the $Ro = 0.5$ cyclone and anticyclone is very similar to the linearly evolving vortex, the later evolution shows some differences. By time $100T_\Omega$ (in figure 2*b*) there appears some three-dimensional variation in the core of the cyclone and also some diminution of the amplitude (presumably because there is some cascade to smaller scales and hence some dissipation of energy). However, the column even at time $100T_\Omega$ is basically intact and primarily two-dimensional. In figure 2(*c*), we see that in the anticyclonic case the evolution is farther from the linear evolution than in the cyclonic case at time $100T_\Omega$. The cyclone is at that time more closely two-dimensional and somewhat stronger than the anticyclone. Note also that the cyclone at $t = 100T_\Omega$ (figure 2*b*) shows a distinct 'sausage mode'. The deformation of the anticyclone at that time is less easy to categorize, but some oscillation persists.

Next we consider the evolution of the initially perturbed tube without background rotation for the same period of time, measured in units of T_e, as in the cases with rotation. Recall that T_e is the same as T_Ω in those cases because there we have $Ro = 0.5$ and so $\Omega = |\omega_0|$. In figure 2(*d*), we see that without background rotation there is little tendency to two-dimensionalize, that is the tube remains somewhat bent as in the initial condition. Also we note that there is no inertial wave activity, as is evident from comparing the early frames here with those in the other rows. By time $100T_e$ there has been significant cascade to small scales. Comparing the infinite Rossby number case to the anticyclonic case with $Ro = 0.5$ we could say that on the small scale the infinite Rossby number case has relatively much more energy in three-dimensional motions. Continued evolution, as we will illustrate later, continues production of three-dimensional variations tending toward a state of isotropic homogeneous three-dimensional turbulence, whereas the cyclone and anticyclone will remain basically columnar.

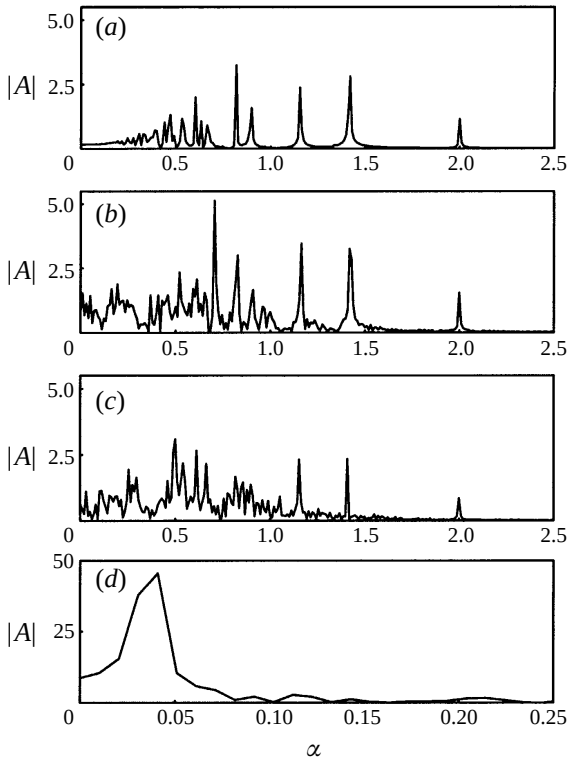

FIGURE 4. Discrete Fourier spectrum of the evolution of the velocity component v in the centre of the domain. The four cases correspond to those illustrated in figure 2: (*a*) linear dynamics, (*b*) cyclone with $Ro = 0.5$, (*c*) anticyclone with $Ro = 0.5$. and (*d*) $Ro = \infty$ ($\Omega = 0$). The time span used to compute the spectrum in each case is the same as in figure 2, $100T_e$. In (*a–c*) this is equal to $100T_\Omega$. Plotted is the modulus $|A|$ of the amplitude of the discrete Fourier transform as a function of the non-dimensional frequency α in units of Ω in (*a–c*), and in units of $|\omega_0|$ in (*d*).

Another way to compare the evolution of these perturbed vortices is to consider the frequency spectrum of the long-term history of some component of the flow. In figure 4, we show the frequency spectra for a period of $100T_\Omega$ of the evolution of the y-component of the velocity (which starts at 0) measured in the centre of the domain for each of the cases shown in figure 2. In figure 4(*a*), where we have plotted the spectrum for the linear evolution, we see a series of well-defined peaks. The frequencies of these peaks all correspond to the frequencies of wavevectors that are originally excited by the perturbation to the basic state. For example, the peaks with non-dimensional frequency α/Ω above 0.5 correspond to the wavevectors listed in table 1. Note that all the excited modes have $|k_z| = \kappa = 1$, i.e. the vertical wavenumber of the initial perturbation. For different values of κ, the frequencies would be different and can be found by replacing $k_z = 1$ by $k_z = \kappa$ in table 1 and recalculating the frequencies using formula (3.4).

Looking at the spectrum for the cyclone with $Ro = 0.5$ in figure 4(*b*) we see that many more low-frequency modes have been excited in comparison to the linear case. These modes result from nonlinear excitations of small-scale modes not found in the initial conditions, and hence not found in the linear dynamics spectrum shown in figure 4(*a*). In the spectrum of the anticyclone with $Ro = 0.5$ shown in figure 4(*c*), we see that the amplitudes, at least at frequencies above $\alpha/\Omega = 1$, are lower than in

α/Ω	(k_x, k_y, k_z)
2.000	(0,0,±1)
1.414	(0,±1,±1), (±1,0,±1)
1.155	(±1,±1,±1)
0.894	(0,±2,±1), (±2,0,±1)
0.816	(±1,±2,±1), (±2,±1,±1)
0.666	(±2,±2,±1)
0.632	(0,±3,±1), (±3,0,±1)
0.603	(±1,±3,±1), (±3,±1,±1)
0.535	(±2,±3,±1), (±3,±2,±1)

TABLE 1. Identification of peaks in the linear frequency spectrum with wavevectors excited in the initial perturbation.

the cyclonic case. Also it appears that there is relatively more power in the lower frequencies in the anticyclonic case. We can calculate the frequency below which more than half of the power in the spectrum is contained. Calling this frequency α_h, we find $\alpha_h = 0.82$, 0.70, and 0.55 for the linear case, the nonlinear cyclone and nonlinear anticyclone, respectively. Thus relative to the linear case, where a cascade of energy to small spatial scales is not possible, in the nonlinear cases additional lower frequencies are excited, but more so in the anticyclonic than in the cyclonic case. The reason for this is not clear at present. Originally, all of the wavevectors that have energy have $k_z = 0, \pm 1$. It is difficult to see how any diffusion in k-space, as in an inertial cascade by nonlinear interaction, could be responsible for transfer to lower frequencies, which for the inertial wave field requires a smaller ratio of $|k_z|$ to k. An understanding of this must come through considering modes on the vortex core itself (as was done by Smyth & Peltier 1994 for the case of a vortex tube in a shear flow) rather than modes about the state of no motion. The test point where the spectrum is measured is the centre of the computational domain which remains near the core of the vortex. This is the region where the fields are strongest and where nonlinear coupling would be the strongest.

We also note that in figure 4(*b*) (the case of the cyclone) there is a large peak around the non-dimensional frequency $\alpha/\Omega \approx 0.70$, which is absent in the spectrum for the anticyclone in figure 4(*c*). This could correspond to wavevector (2,5,2) or (5,2,2) with any combination of signs for the components. This wavevector could be produced by the nonlinear interactions of the following pairs of wavevectors that are present in the initial data: (1,4,1) and (1,1,1), (2,2,1) and (0,3,1), and (2,3,1) and (0,2,1) (with interchanges in k_x and k_y possible and various sign combinations). Of the three possible triads that can be made with these modes, only the triad (1,4,1),(1,1,1),$(-2,-5,-2)$ is resonant, that is the corresponding inertial wave frequencies sum to zero, and hence it is a good candidate for a strong interaction that could produce the peak in question. On the other hand, since the spectrum is measured near the core of the vortex, this peak may be due to an oscillation of the core such as the 'sausage mode' we see in figure 2(*b*) at $t = 100T_\Omega$. In either case, it is curious that this peak is missing in the anticyclonic case, and any explanation would have to account for that.

The result for the infinite Rossby number case ($\Omega = 0$) is shown in figure 4(*d*). Note that the scales are different from those in figure 4(*a–c*). Here all of the excitation is in the frequency band [0,0.25], that is all of the excitation is at very low frequency in comparison to the rotating case with $\Omega = 0.5$.

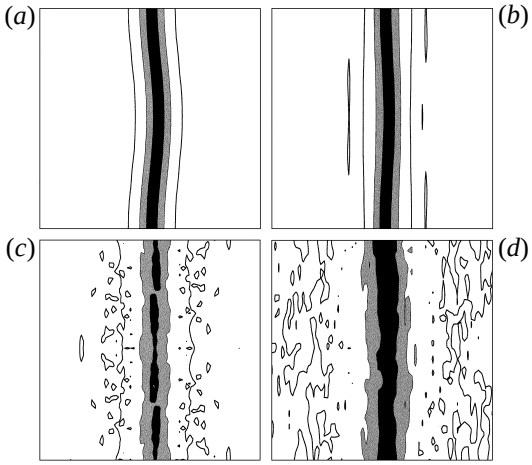

FIGURE 5. Shaded contours of $|\omega|$ in a (y, z)-cross-section, for the evolution of the cyclone with a small three-dimensional perturbation and initial Rossby number $Ro = 5$. The contour levels in (a–c) are (0.025, 0.4 and 0.8) ω_0, with the (grey) black areas having values above (0.4) 0.8 ω_0. The contour levels in (d) are (0.0125, 0.15 and 0.3) ω_0, with the grey (black) area indicating values above 0.15 (0.3) ω_0. The times are (a) $t = 0$, (b) $t = 2T_\Omega$, (c) $t = 10T_\Omega$ and (d) $t = 100T_\Omega$ (spatial resolution 64^3).

6.2. *Large Rossby number*

Although we have seen some results for very large Ro, that is $Ro = \infty$, this is not representative of the case of the cyclone at moderately large Ro, i.e. a slowly rotating case. We have simulated the evolution of the tube with small perturbation with finite Rossby numbers ranging up to $Ro = 78$. We varied the value of Ro by varying ω_0 with the value of Ω, and hence T_Ω, held fixed. We will discuss in detail the case of $Ro = 5$ as representative of slow rotation.

In figure 5 we show the evolution of the $Ro = 5$ weakly perturbed cyclone. The early evolution, for times up to a few rotation periods, is similar to the $Ro = 0.5$ case; however, by time $t = 10T_\Omega$, we note significant buildup of small-scale three-dimensional distortions to the tube. The development of the three-dimensional variability causes enhanced decay of the vortex amplitude in comparison with the low Rossby number case. Nevertheless, the cyclone still persists. By $t = 100T_\Omega$, although the core has lost some amplitude and is suffering from some three-dimensional perturbations (note that the contour levels plotted in figure 5(d) are lower than in the previous panels), the vortex remains a robust structure with peak amplitude that implies a Rossby number of 2.2, well above the $Ro = 1$ level.

In the case of the anticyclone (see figure 6), the vortex is badly disrupted near $t = 2T_\Omega$. After that the core is not seen at the amplitude level above $0.4\omega_0$, although still visible at lower contour levels. For example, at time $t = 10T_\Omega$ which corresponds to figure 6(c), isosurface plots of vorticity magnitude reveal a continuous tube but only for contour levels below $0.2\omega_0$. Comparing figure 6(d) (at reduced contour levels) here with the corresponding panel for the cyclonic case (figure 5), we see that the core of the cyclone is better preserved, but we also note that the core of the anticyclone at this time is reasonably well defined albeit at a lower amplitude. In fact, the peak amplitude of the vertical vorticity component of the anticyclone is about $|\omega_z| = 0.16|\omega_0|$. This corresponds to a new Rossby number of 0.18 of the original value, which gives a new Rossby number of 0.8. In a sense, we can consider the core

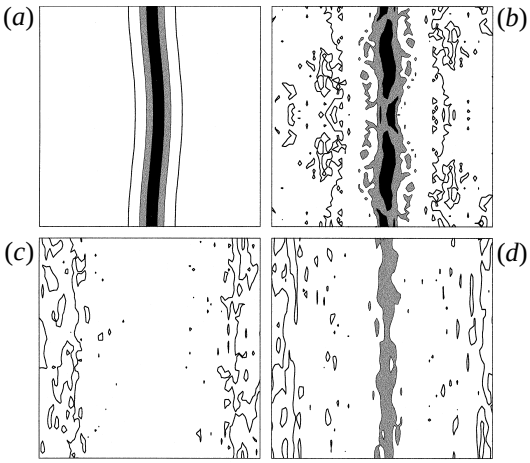

FIGURE 6. As figure 5 but for the evolution of the anticyclone. The contour levels in (*d*) are 0.0125 and 0.15 ω_0, with the grey area having values above 0.15 ω_0. The times are (*a*) $t = 0$, (*b*) $t = 2T_\Omega$, (*c*) $t = 10T_\Omega$ and (*d*) $t = 100T_\Omega$ (spatial resolution 64^3).

to have decayed to a point where it is centrifugally stable. That is, its Rossby number based on the evolving peak amplitude has fallen to a level below the threshold for centrifugal instability.

This is a rather remarkable result for the evolution of the high-Rossby-number anticyclone. The centrifugal instability that it undergoes involves overturning, and the three-dimensional turbulence that results is nearly isotropic. Nevertheless, in the long term the flow does result in a 'stable' ($Ro < 1$) anticyclone. One may question whether or not this same result would be obtained if the resolution were higher allowing more small-scale activity. To test this, we performed a long-term integration of the $Ro = 5$ anticyclone at resolution 128^3. The resulting evolution was essentially the same as shown in figure 6.

The temporal evolution of the enstrophy and energy in the 128^3 simulation, shown in figures 7(*a*) and 7(*b*), respectively, also provides clues to the evolution. Both the case of the anticyclone (solid line) and the cyclone (short-long dashed line) are shown. For the cyclone, the energy and enstrophy are approximately conserved. For the anticyclone, the enstrophy begins to grow slowly at first and then very rapidly, reaching a peak at about thirteen times its initial value at time $t = 3T_\Omega$. After this large burst due to the centrifugal instability, the enstrophy decays rapidly with some minor fluctuations later in time, but after $t = 15T_\Omega$ the decay is monotonic. The energy for the anticyclone is nearly constant in the initial phase of the instability. During the period of high enstrophy, the energy decay is correspondingly rapid. For long times, $t > 15T_\Omega$, the energy decay becomes slow and nearly linear. Also in figure 7, the energy and enstrophy histories are shown for the anticyclone that result from a simulation at a lower resolution of 64^3 (the results for the cyclone were unchanged at the lower resolution). Note that with the Kraichnan eddy-viscosity model, energy dissipation is not simply proportional to total enstrophy, unlike the case in simulations with only Laplacian viscosity, because the Kraichnan eddy-viscosity is not independent of the wavenumber k. At lower resolution the peak enstrophy is diminished because smaller-scale motions are not resolved, and yet the energy decay rate during the period of increased enstrophy is not greatly changed by this variation in the resolution.

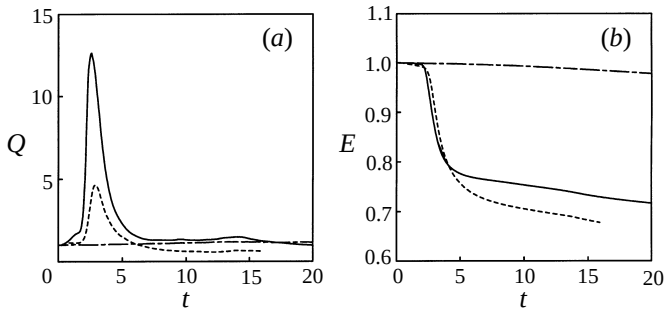

FIGURE 7. History of (*a*) total enstrophy Q and (*b*) total energy E, both normalized by their initial values, for the $Ro = 5$ weakly perturbed anticyclone (solid curve) and the weakly perturbed cyclone (short-long dashed curve) in simulations with resolution 128^3. The dashed curve shows the result for the anticyclone at resolution 64^3. Time is in units of the rotation period T_Ω.

It is also interesting to compare the evolution of energy spectra for both cyclone and anticyclone. In figure 8, we see instantaneous plots of the energy spectra at times from $t = 0$ to $t = 30T_\Omega$ at intervals of $3T_\Omega$ (thicker curves correspond to earlier times). For the cyclone (figure 8*a*), we see that although there is some transfer of energy to small scales, the energy in the large scales remains fairly constant and there are about four orders of magnitude difference between the energy at the largest and smallest scales. Also the small-scale energy spectrum is nearly flat (white). In contrast, for the anticyclone (figure 8*b*), there is a strong transfer of energy from the large to the small scales evident at $t = 3T_\Omega$. The energy in the smallest scales is then only about two orders of magnitude smaller than that in the largest scales. By $t = 9T_\Omega$, the small-scale spectrum (from about $k = 7$) is nearly a $k^{-5/3}$ spectrum. From about $t = 12T_\Omega$ to about $t = 14T_\Omega$ the amplitude of the $k^{-5/3}$ part of the spectrum grows slightly (corresponding to the slight rise in enstrophy during that period as seen in figure 7*a*), and then decays in time while preserving its $k^{-5/3}$ form until about $t = 25T_\Omega$. After that the shape for $k > 7$ is distorted, perhaps being better represented by two slopes with the spectrum only at the highest values of k being close to the $k^{-5/3}$ form.

If we consider the form of the Kolmogorov spectrum

$$E(k) = K_o \epsilon^{2/3} k^{-5/3} \tag{6.1}$$

with K_o the Kolmogorov constant and ϵ the rate of energy decay, we can check to see how close these spectra come to that for decaying non-rotating turbulence. Estimating ϵ from the energy curve and comparing values of $E(k)$ in the small-scale inertial range, we have estimated, from the curves shown in figure 8(*b*), values of K_o in the range [0.25,0.35]. These values are somewhat lower than those in the range of typical results for isotropic turbulence (see for example Grant, Stewart & Moilliet 1962 who give $K_o = 1.44$, or Leslie 1973 for a review).

For the case $Ro = \infty$, that is $\Omega = 0$, the vortex at time $t = 100T_e$ showed no tendency to relax and was developing strong small-scale three-dimensional fluctuations in the core (as shown in figure 2*d*). From that point on, the flow becomes very three-dimensional and isotropic with vorticity levels falling rapidly. This is illustrated in figure 9 where we see a cross-section of the absolute value of the vorticity represented with one shaded contour level. In figure 9(*a*) the time is $t = 100T_e$ and the contour level is $0.6\omega_0$. By $t = 300T_e$, as shown in figure 9(*b*), with contour level $0.06\omega_0$, the flow has isotropized. A similar image is still seen at $t = 1000T_e$ (not shown)

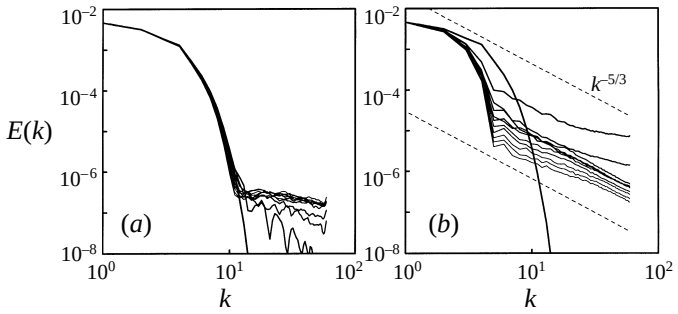

FIGURE 8. Energy spectrum evolution for the $Ro = 5$, weakly perturbed (a) cyclone and (b) anticyclone. The spectrum is shown at intervals of $3T_\Omega$ from $t = 0$ to $t = 30T_\Omega$. The thickness of the curves indicates the sequence of time with thicker curves corresponding to earlier times. $E(k)$ is the total of the energy in all the modes with wavenumbers greater than $k - 1$ and less than or equal to k (i.e. $E(k)$ is the isotropic energy spectrum). The dashed curves indicate the slope of the Kolmogorov $k^{-5/3}$ spectrum.

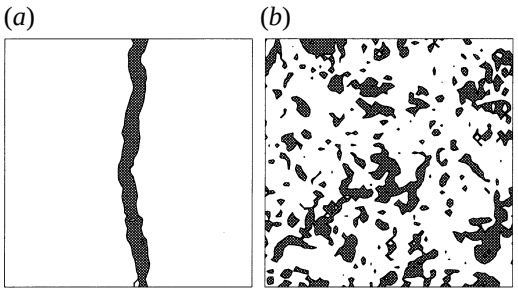

FIGURE 9. Shaded contours of $|\omega|$, in a (y, z) cross-section, for the case $\Omega = 0$: (a) time $t = 100T_e$ with contour level at $0.6\omega_0$, (b) time $t = 300T_e$ with contour level at $0.06\omega_0$, ($T_e = 2\pi/\omega_0$).

but at contour level $0.012\omega_0$. This is to be contrasted with the well-defined columns still surviving at time $t = 100T_\Omega = 1000T_e$ for $Ro = 5$ in the rotating environment (see figures 5*d* and 6*d*). A three-dimensional view of the vorticity field after about $t = 200T_e$ shows that the field is composed of many small-scale elongated vortices (cf. Vincent & Meneguzzi 1991).

In figure 10 we show the frequency spectra of the evolution at $Ro = 5$. The linear dynamics reproduces the spectrum shown figure 10(a), which is of course the same as in figure 4(a), but at a higher amplitude because ω_0 has been increased by a factor of 10 while Ω has been held fixed at the value 0.5. The nonlinear simulations, as one might expect, give very different frequency spectra for the $Ro = 5$ cyclone and anticyclone cases. What is perhaps surprising is that the cyclone produces the spectrum shown in figure 10(b), which is very different from the linear spectrum and the small-Rossby-number spectrum shown in figure 4(b). There are now only two dominant peaks: one slightly above the inertial frequency, $f = 2\Omega$, and another at approximately 1.5Ω. Perhaps one can consider these as shifted versions of peaks in the linear dynamics spectrum, but it may be more useful to consider modes that can be supported by the vortex tube. All of the other peaks contained in the small-Rossby-number spectrum shown in figure 4(b) are no longer distinguishable here. There seems to be a broad background of noise which extends from 0 up to about 10Ω (not fully shown here) with no sharp cutoff. For the anticyclone, we see in

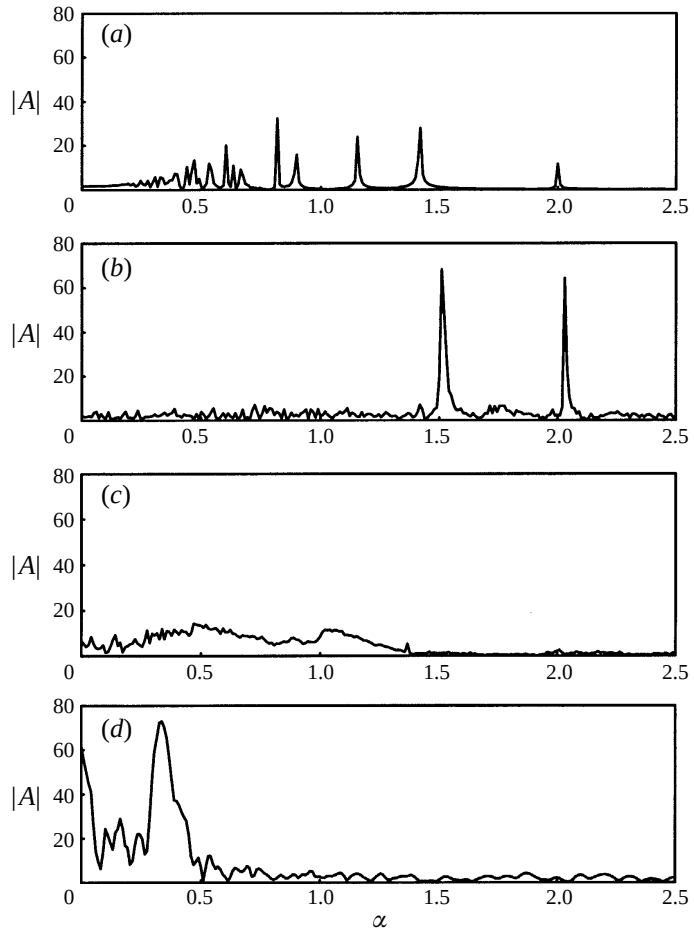

FIGURE 10. Discrete Fourier spectrum of the evolution of the velocity component v in the centre of the domain, for (a) linear dynamics, (b) cyclone with $Ro = 5$, (c) anticyclone with $Ro = 5$, and (d) $Ro = \infty$ ($\Omega = 0$ and $\omega_0 = 5$). The length of the record analysed in each case is $100 \times 4\pi = 1000T_e$ which corresponds to $100T_\Omega$ in (a–c). Plotted is the modulus $|A|$ of the amplitude of the discrete Fourier transform as a function of frequency α in units of Ω in (a–c), and in units of $\omega_0/10$ in (d).

figure 10(c) just a noisy background with none of the peaks seen in the small Rossby number case shown in figure 4(c). The frequency spectrum for the case of infinite Rossby number with $\omega_0 = 5$ is shown in figure 10(d). To compare with the spectrum for the analogous case at $\omega_0 = 0.5$ in figure 4(d), we have scaled the frequency by a factor of 10 (corresponding to the tenfold increase in the vorticity amplitude). In fact, the spectrum in figure 4(d) could be considered just the spectrum of the early period of the evolution with figure 10(d) showing the long-term spectrum, because the difference between the two runs is mostly a matter of time scaling. In addition to the dominant low-frequency peak that appears in both figures, there is an additional peak at zero frequency in figure 10(d) coming from the long-term trends.

As a quantitative measure of the degree of anisotropy in the flow field we have calculated the ratio of the total enstrophy in the component ω_z to the total enstrophy. This leads to a fairly noisy signal, but we find that by conditioning the sums such that only points where the vorticity exceeds in magnitude one half the maximum vorticity

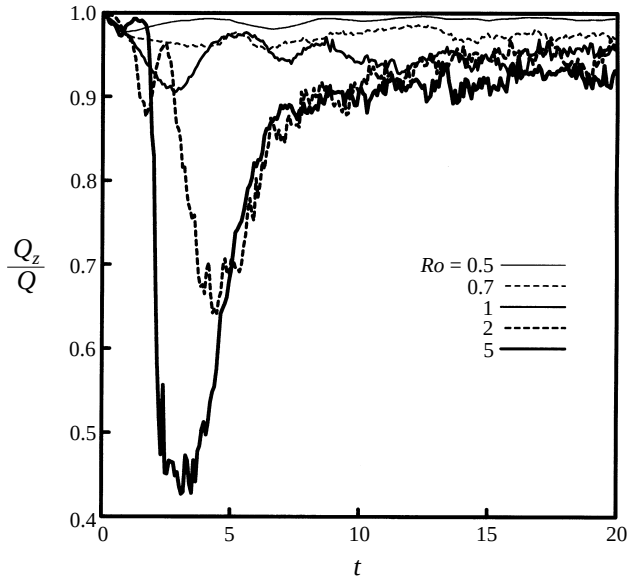

FIGURE 11. The ratio of z-enstrophy Q_z, to total enstrophy Q, with the condition that only vorticity of magnitude above half the peak vorticity is considered (see (6.2) and (6.3)). Anticyclonic initial conditions with various Rossby numbers as indicated. Time is in units of T_Ω.

magnitude for the whole field, we produce a smoother signal, more representative of the condition of the vortex tube than the small-scale small-amplitude field. In figure 11 we show the evolution of Q_z/Q, where we define

$$Q_z = \sum{}' w_z^2, \tag{6.2}$$

and

$$Q = \sum{}' w_x^2 + w_y^2 + w_z^2. \tag{6.3}$$

The prime on the summation sign indicates that the sums are taken over the set of points such that $|\omega| \geqslant 0.5 \max\{|\omega|\}$. The value $Q_z/Q = 1$ corresponds to the case of columns with no z-dependence, while the value $Q_z/Q = 1/3$ corresponds to the case of isotropic three-dimensional turbulence. In figure 11 we show only the results for anticyclones. For cyclones the signal always remains close to 1 even for $Ro = 5$. We have actually performed simulations for many more Rossby numbers intermediate to and beyond the range of the five cases shown in figure 11, but these five are representative. These results show that although the Rayleigh criterion is based only on the consideration of axially symmetric overturning motions, it is nevertheless a useful indicator of the stability of vortex tubes subjected to three-dimensional perturbations and background rotation, as was previously concluded by Smyth & Peltier (1994).

For anticyclones with $Ro < 1$, the value of Q_z/Q remains close to 1, although there is some temporary decrease initially. Thus it seems that the deviation away from the pure z-independent case grows initially for the anticyclones, if only temporarily, even in cases with $Ro < 1$. For $Ro > 1$ anticyclones, we see major decreases in the value of Q_z/Q in the first few rotation periods of the evolution. This was to be expected from the point of view of centrifugal instability. The most surprising thing is that there is

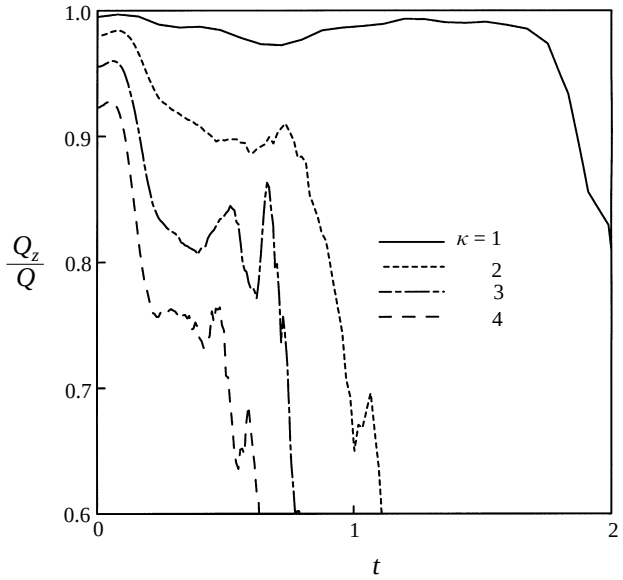

FIGURE 12. The ratio of Q_z to Q, with only vorticity of magnitude above half the peak vorticity considered (see (6.2) and (6.3)). An anticyclone with Rossby number $Ro = 5$ with an initial perturbation with vertical wavenumbers $k_z = \kappa$ as indicated. Time is in units of T_Ω.

then an adjustment in which Q_z/Q grows, eventually saturating at a value close to 1. Furthermore, there are certain systematic trends as a function of the Rossby number. Regarding the period of instability and isotropization, increasing the Rossby number decreases the time on the t/T_Ω scale at which the instability commences, increases the rate of the decay of Q_z/Q, and lowers the minimum value of Q_z/Q reached. For the later evolution, increasing the Rossby number increases the length of time for the return of Q_z/Q toward 1 and decreases the final value of Q_z/Q that is achieved asymptotically. We have tested whether these trends continue for larger Ro and found this to be the case for all values tested which included values up to $Ro = 78$.

It is difficult to infer from figure 11 how the early growth rates of instability depend on the Rossby number. The early behaviour is complicated due to the presence of transients. Additional experiments at lower resolution of 32^3 gave essentially the same results as shown in the figure. Smyth & Peltier's (1994) results suggest that there is not much variation in growth rates of the most unstable modes in the linear dynamics as the Rossby number varies upwards from about $Ro = 2$ for $\kappa = 1$ (see discussion at the end of §4).

The results shown so far were all for the case of $\kappa = 1$. In figure 12 we show the early evolution of Q_z/Q at $Ro = 5$ for different vertical wavenumbers κ for the initial perturbations. Figure 12 indicates that as the vertical wavenumber increases the rate of isotropization increases. This appears to be in accordance with the linear stability calculations of Smyth & Peltier (1994) for the case of the elliptical vortex in a shear flow (see further remarks at the end of §4).

In figure 13 we make a comparison between the $Ro = 5$ case and much higher Rossby numbers. Here we consider an anticyclone with $Ro = 78$ and the infinite Rossby number case ($\omega_0 = 5$ and $\Omega = 0$). The value of $Ro = 78$ was chosen because this is the largest Rossby number that could be accommodated and still have the entire unstable range, $r_1 < r < r_2$ (see §3.2), within the computational domain. At $Ro = 78$,

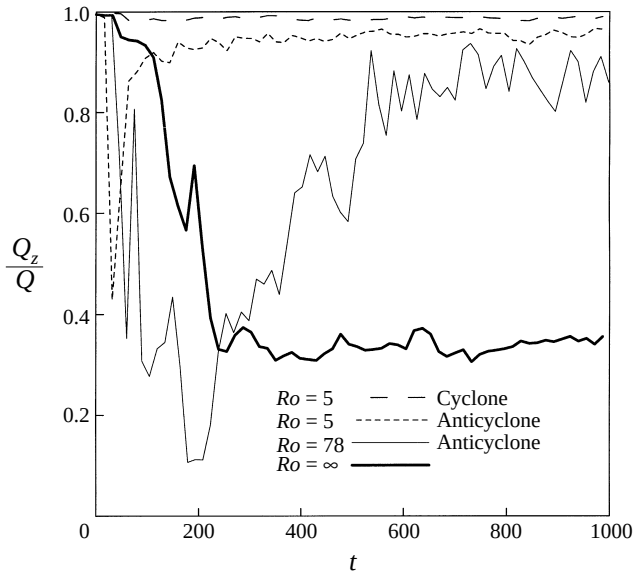

FIGURE 13. The ratio of Q_z, to Q, with only vorticity of magnitude above half the peak vorticity considered (see (6.2) and (6.3)). The $Ro = 5$ cyclone, the $Ro = 5$ anticyclone, the $Ro = 78$ anticyclone and the $Ro = \infty$ vortex. Time is in units of the eddy turnover time $T_e = 2\pi/|\omega_0|$.

we see that Q_z/Q actually falls below the isotropic value of $1/3$ before returning to higher values. Also, for such high Rossby numbers, the final anisotropic state is no longer dominated by an anticyclone, but rather the result is a cyclone surrounded by a more-diffuse less-intense anticyclonic vorticity. It appears that between $Ro = 25$ and $Ro = 50$ there is a gradual transition, as the Rossby number is increased, in which the final state becomes dominated by a cyclone instead of an anticyclone. Thus Q_z/Q approaching 1 in the $Ro = 78$ case represents the two-dimensionalization of the resulting cyclone.

In the infinite Rossby number case, the measure of anisotropy falls to approximately $1/3$ and fluctuates there as expected in a return to isotropy. Unlike the cases with background rotation, here there is no return toward the anisotropic state (i.e. no Taylor column formation). Note that in figure 13 we have plotted the evolution with time scaled by the eddy time scale $T_e = 2\pi/\omega_0$. In terms of scaling with $T_\Omega = 2\pi/\Omega$, we found that the minimum in Q_z/Q occurs earlier for larger Ro. The trend is not entirely monotonic when the data are scaled by $T_e = 2\pi/\omega_0$, but roughly speaking the larger Ro, the later the minimum occurs.

With the $Ro = 78$ case, we can also illustrate the early evolution of the centrifugal instability better than in the $Ro = 5$ case. The smaller Ro, the closer the instability region is to the centre of the vortex. For example, at $Ro = 5$, the inner radius of the instability range is $r_1 \approx 1.8\sigma$ (see §3.2) corresponding to a vorticity level of $|\omega| \approx 20\%|\omega_0|$. Thus, when breakdown occurs, it rapidly involves the entire vortex, and it is difficult to discern the different spatial regions involved. On the other hand, at $Ro = 78$, we have $r_1 \approx 3.0\sigma$, which corresponds to a vorticity level of $|\omega| \approx 1.3\%|\omega_0|$. Since the instability region is outside the region of strong vorticity, it is easier to describe the early progress of the instability in this case. In figure 14(*a*), we show two views of the early evolution of an isosurface ($|\omega| = 1.4\%|\omega_0|$), which is essentially on the border between the regions where the left-hand side of (3.7) in our generalized

Rayleigh criterion changes sign. The isosurface is coloured by the value of ω_z on the surface. At time $0.16T_\Omega$, from the side view, we see that there has been a good deal of activity on this isosurface, with the creation of cyclonic vorticity well within the instability range. Most of the overturning motion initially occurs in the regions where the tube axis is most inclined away from the z-axis. From the top view, at $t = 0.16T_\Omega$, we see that this activity results in spiral bands of cyclonic vorticity around the core, while the core itself appears preserved from intrusions of the $|\omega| = 1.4\%|\omega_0|$ isosurface. This is similar to the findings of Smyth & Peltier (1994) that the fastest growing mode for an elliptical vortex in a shear flow was what they called the 'edge mode', which manifests itself in the annulus around the core where the Rayleigh criterion (3.7) would allow instability.

A very short time later (see $t = 0.2T_\Omega$), the isosurface has filled the entire instability range (for $Ro = 78$, $r_2 \approx \pi$), while the core region is still essentially free of this isosurface. In figure 14(*b*), we show the comparison with the evolution of the $|\omega| = 2.8\%|\omega_0|$ isosurface, which lies deeper in the core region. At time $0.16T_\Omega$, this isosurface is less perturbed than the lower-value isosurface. The main activity again is in the region where the tube is most inclined away from the z-axis. By time $t = 0.2T_\Omega$, this isosurface has extended significantly into the instability region, but not to the degree that the lower-value isosurface has. Also note that for both isosurface values, at $t = 0.2T_\Omega$ most of the activity appears at values of z corresponding to the regions where the tube was most aligned along the z-axis, in contrast to the earlier evolution. Overall, a picture is suggested in which the instability begins near the inner radius of the instability region with activity systematically spreading out through the instability region. As time proceeds the core also becomes involved in the instability. This is born out by examination of the evolution of higher-level isosurfaces than those shown here.

7. Large perturbations

In the previous section we considered the effect of relatively small, but three-dimensional, perturbations on the evolution of the vortex column. In that case, linear theory, and to a certain extent Rayleigh stability theory, were useful guides to understanding the evolution. Now we turn to the question of large perturbations where we will see that these theories are still somewhat useful although nonlinear effects eventually dominate.

Again, we choose as our basic state the Gaussian vorticity distribution (3.8), and we create the perturbed state as in equation (4.2), but in contrast to the weak perturbations used above, here we take a perturbation that is 10 times stronger, with $y_f = t_f v_0/\sigma = 8$. With a perturbation this large, the distance that the vortex axis is initially displaced from the z-axis is larger than the vortex core size. As we will see, the tendency of the misaligned parts of the vortex tube to two-dimensionalize separately will cause strong stretching and twisting of the vortex tube.

7.1. *Small Rossby number*

We begin by looking at the case of the strongly perturbed cyclone with $Ro = 0.5$. In figure 15(*a*), we show the evolution in the fully nonlinear dynamics. The structures shown are isosurfaces of vorticity of constant magnitude viewed along a horizontal axis. The orientation of the viewing axis is chosen in each frame to show the maximum distortion of the tube at that time. The isosurfaces are coloured according to the value of the vertical vorticity, ω_z, on the isosurface, with a spectrum of colours running

from red to blue (red/blue for positive/negative values). The evolution begins with a decrease in the degree of bending. After only about one third of a rotation period, however, we see that the vortex tube has been twisted in such a way that there are now two sections antiparallel to the initial orientation. These sections with negative ω_z are sandwiched between the segments of the tube with positive ω_z. Thus four loops have been formed in the original structure. Although not shown here, it turns out that the helicity of the adjacent loops form cancelling pairs. That is, the helicity for the two upper loops is such that they form a pair of opposite helicity, and similarly for the two lower loops. As time proceeds, the segments of negative ω_z are stretched and become very thin (see figure 15*a* at $t = 0.57T_\Omega$). The segments of positive ω_z begin to touch and merge to form two tubes that stretch through the whole domain, and the negative segments become so thin that they are no longer resolved (see figure 15*a* at $t = 1.9T_\Omega$). The two tubes then begin a complicated interaction, merging in some sections faster than in others, but with an eventual outcome of a single tube albeit with pervasive small-scale structures. On the large scale, the structure shown at $t = 19.1T_\Omega$ is largely independent of z. However, small-scale structures permeate the whole as we can see in the two-dimensional cross-section shown in figure 15(*b*). Only a portion of the computational domain is shown in the cross-section. The colour table on the right of the figure indicates the quantitative assignment of colours for the ω_z field.

We have repeated this simulation with a variety of types of dissipation. A run with hyperviscosity and a purely inviscid run show results very similar to those shown in figure 15. Direct numerical simulations (i.e. where only Laplacian viscosity is used) at resolution 64^3 also show very similar behaviour up to time $t = 0.57T_\Omega$; however, after that there are significant differences since the vorticity amplitude falls off rapidly on all scales. The Laplacian viscosity that is necessary to avoid accumulation of energy at the highest wavenumber at practical resolutions is too large to allow the final stages of the vortex evolution to be comparable to that in high-Reynolds-number flow.

It is interesting to consider the evolution of the z-vorticity field in a cross-sectional cut through one of the two double-loop regions shown in figure 15(*a*). This is shown in figure 16. At time $0.3T_\Omega$ the loop structure shows its signature in the cross-section as a tripolar vorticity field (two cyclonic satellites and an anticyclonic core, see van Heijst, Kloosterziel & Williams 1991). Unlike the pure two-dimensional evolution of the tripole (Carton & Legras 1994), the core is soon stretched in the z-direction and hence the area is thinned out until it is no longer resolved. At time $t = 1T_\Omega$ we see evidence of multiple cyclonic tubes. The evolution from about time $t = 1.9T_\Omega$ until $t = 6.4T_\Omega$ is similar to the two-dimensional merger of two cyclones (Melander, Zabusky & McWilliams 1988). The subsequent evolution, although similar to two-dimensional axisymmetrization on the large scale, is three-dimensional on the small scale. Purely inviscid simulations show essentially the same results, with some additional energy at small scales.

Some of the above behaviour can be ascribed to purely linear effects. Until about the point shown in figure 15(*a*) at $t = 0.57T_\Omega$, the purely linear (not shown) and the nonlinear evolutions are very similar. So the formation of the initial loops including the creation of the antiparallel sections of the tube is a purely linear effect. Therefore, in principle it is possible to analyse this loop formation with linear radiation theory as discussed in §3, although to describe it analytically is by no means a simple matter. The subsequent behaviour in which parts of the tube merge together almost as in two-dimensional vortex dynamics is, however, the result of nonlinear processes. To emphasize this, we show in figure 17 the result of the linear evolution at the time

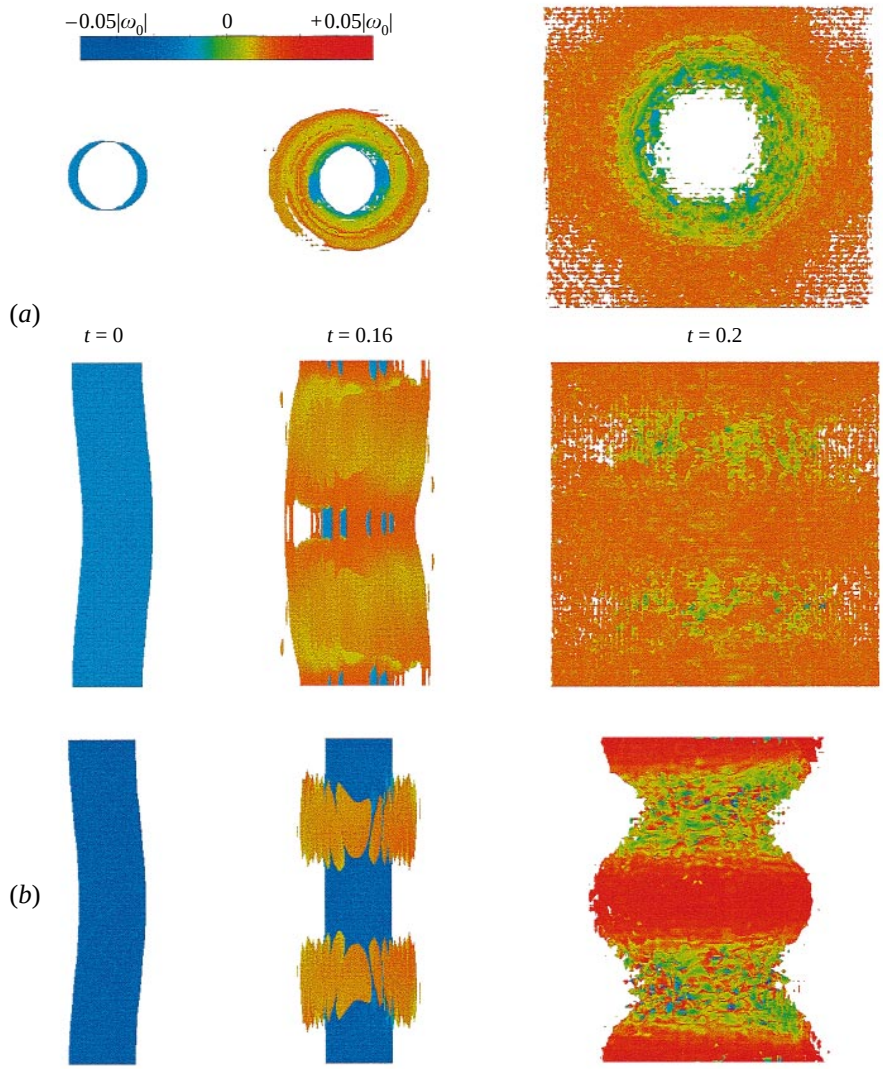

FIGURE 14. Illustration of the early evolution of the $Ro = 78$ weakly perturbed anticyclone. (*a*) Two views of the $|\omega| = 0.015|\omega_0|$ isosurface are shown: the top line is from above, along the z-axis; below is from the side, along the x-axis. (*b*) The evolution of the $|\omega| = 0.028|\omega_0|$ isosurface in a side view. The colours indicate the value of ω_z on the isosurface. Times are in units of T_Ω.

$t = 19.1T_\Omega$. Two perpendicular views of the 'tube' are shown. The z-axis is the same in each view, but in figure 17(*a*), the y-axis is in the plane of the page while in (*b*) the x-axis is in the plane of the page. Only a greyscale plot is necessary because at this time all points on the isosurface have positive ω_z. The structure is highly anisotropic on the large scales, unlike the corresponding tube shown at this time in figure 15(*a*). Thus, nonlinearities clearly are an important ingredient in the adjustment to the quasi-two-dimensional state. The nature of these nonlinear effects is at this point not well understood. We know of some purely nonlinear mechanisms which may come into play in producing the Taylor column. For example, the two-dimensional merger of

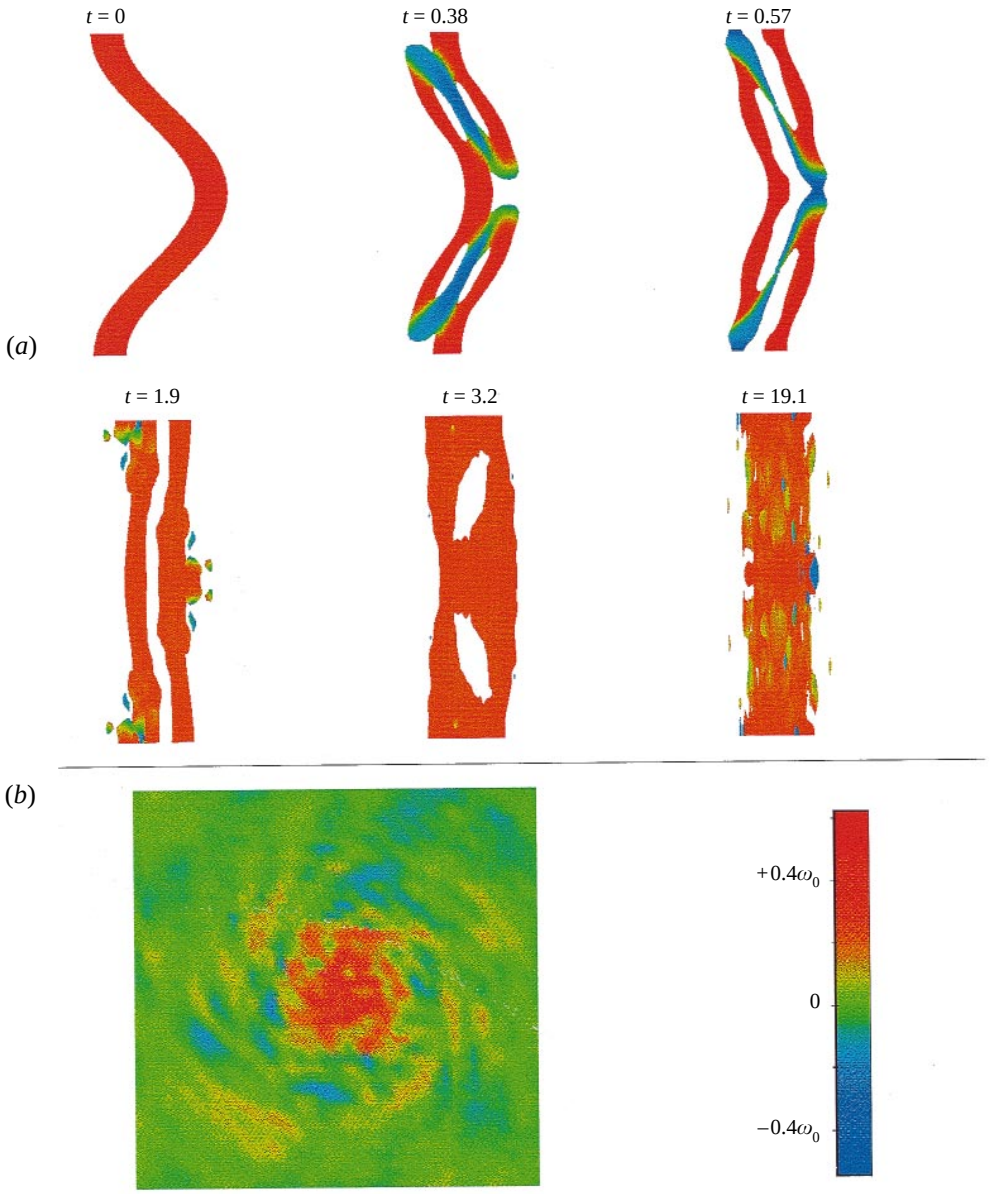

FIGURE 15. Evolution of the strongly perturbed $Ro = 0.5$ cyclone. (*a*) Isosurface plots of $|\omega|$ illustrating the evolution of the strongly perturbed $Ro = 0.5$ cyclone. The isosurface value is $0.43\omega_0$ for $t \leqslant 0.57$ and $0.25\omega_0$ subsequently. (*b*) Field of ω_z from a horizontal cross-section of the vortex column at time 19.1. Times are in units of T_Ω. The surfaces are coloured according to the value of ω_z as indicated by the colour bar.

like-signed vortices (cf. Melander *et al.* 1988; Carnevale *et al.* 1991) can take nearly parallel pieces of vortex tubes and merge them, thus promoting homogenization and isotropization (cf. Melander, McWilliams & Zabusky 1987) in the horizontal. However, the three-dimensional character of the result in the nonlinear case suggests that this is not a complete explanation. Also, it seems that vortex reconnection must play a role (eg. Melander & Hussain 1989).

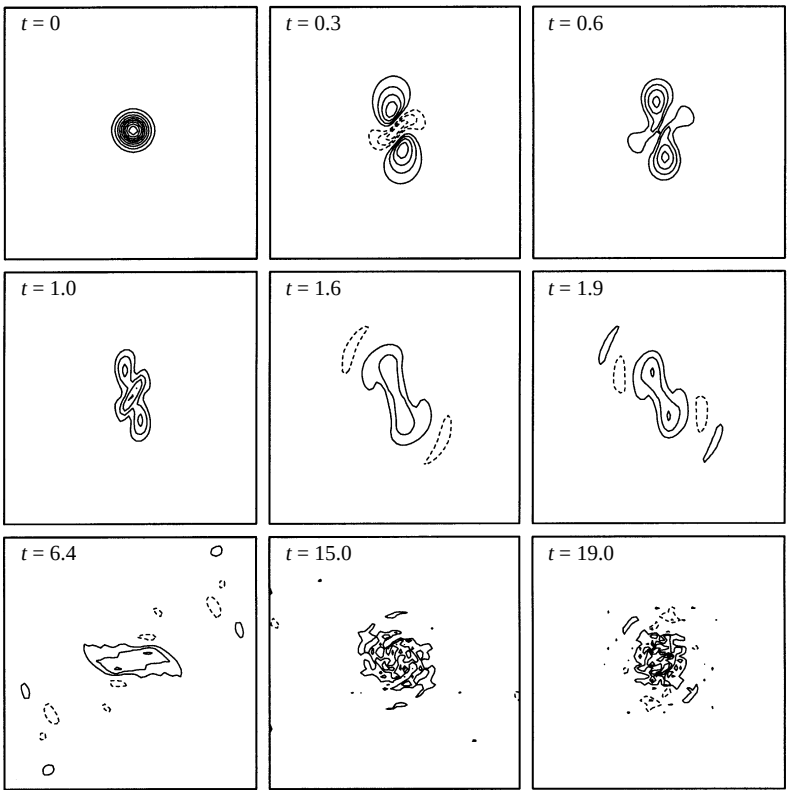

FIGURE 16. Cross-sectional contour plot of the z-vorticity in a plane perpendicular to the z-axis through the uppermost loop region shown in figure 15(*a*). With z running from $-\pi$ to $+\pi$, the cross-section is taken at $z = \pi/2$. Contour intervals are fixed at $0.1\omega_0$. Solid/dashed lines indicate positive/negative ω_z. Time is measured in units of the rotation period T_Ω.

In the case of the strongly perturbed $Ro = 0.5$ anticyclone, there is an initial tendency for the size of the perturbation to increase. However, in a very short time, the creation of loops and antiparallel vorticity takes over much as in the cyclonic case. The subsequent evolution is also similar to the cyclonic case.

7.2. *Large Rossby number*

Next we consider the strongly perturbed $Ro = 5$ case. The very early evolution of the strongly perturbed $Ro = 5$ cyclone is similar to the evolution in the $Ro = 0.5$ case shown in figure 15(*a*) in that there is a tendency for the magnitude of the deviation from the axis to decrease, and there is a distortion of the vortex on the portion inclined at an angle to the rotation axis. As in the $Ro = 0.5$ case, the distortion here begins to produce anticyclonic vorticity in that segment. However, in the $Ro = 5$ case, nonlinear effects are felt very early, and there is no development of the double-loop structure (compare figure 15*a*), which is primarily a linear effect. The early evolution is depicted in figure 18(*a*). Here again the isosurface of $|\boldsymbol{\omega}|$ is viewed along a horizontal axis with orientation chosen in each frame to show the maximum distortion of the vortex and the surfaces are coloured according to the value of ω_z on the surface, with red/blue indicating positive/negative ω_z. We see in this figure the rapid relaxation of the deviation from the rotation axis, then the distortion of the tube primarily on the inclined sections of the vortex with the formation of anticyclonic vorticity, followed

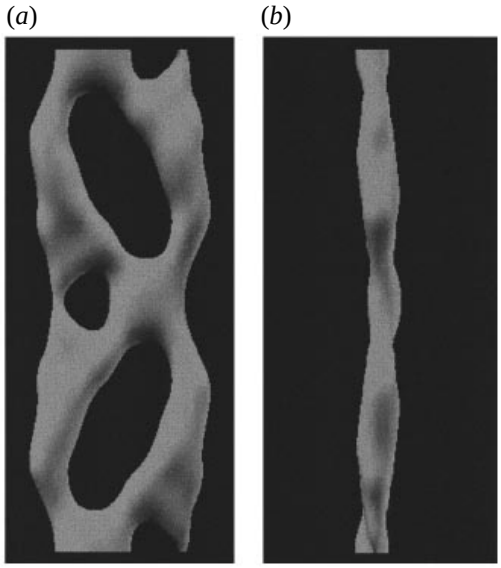

FIGURE 17. Greyscale plot of $|\omega| = 0.25\omega_0$ isosurface resulting from the linear evolution of the strongly perturbed cyclone with $Ro = 0.5$. The time represented is $t = 19.1T_\Omega$ (compare with the nonlinear case in figure 15*a*). Two orientations are shown: (*a*) the view along the *x*-axis and (*b*) the view along the *y*-axis. 'Directional lighting' is used to highlight the three-dimensionality of the structure.

by relaxation toward a structure more nearly aligned with the rotation axis and the loss of the regions of strong anticyclonic vorticity. The last panel in figure 18(*a*) shows signs of a 'sausage mode' on the cyclonic tube at $t = 0.8T_\Omega$, although this does not persist. In fact, in the long run a 'bending mode' dominates. As with the case of the weakly perturbed $Ro = 5$ vortex (see figure 10), the high-frequency large-scale perturbations are not entirely lost, although they are diminished in amplitude. This is evident in the greyscale images of the long-term evolution of the cyclone that are shown in figure 19. In each plot in figure 19, the *z*-vorticity on the surface was only positive. We have reproduced the initial condition to emphasize that the size of the perturbation has diminished, and we have chosen the viewing angle at each time to show the strongest deviation from the vertical that can be seen. The bend continues to form, disappear, and re-form at a frequency close to, but above, the inertial frequency $f = 2\Omega$, i.e. at $\alpha \approx 2.03\Omega$. This is close to the super-inertial frequency peak we saw in figure 10(*b*) for the weakly perturbed cyclone with $Ro = 5$.

Finally, we address the case of the strongly perturbed high-Rossby-number anticyclone. We begin with the strongly perturbed anticyclone ($Ro = 5$) shown in figure 18(*b*). In this figure, the plots are from the results of a simulation at resolution 64^3. In the early evolution ($t < 0.2T_\Omega$), the size of the deviation from the rotation axis increases and the portions of the tube that are not parallel to the ambient rotation axis thicken. By time $t = 0.3T_\Omega$, the portions not parallel to the ambient rotation axis become more three-dimensional in character, with the creation of cyclonic vorticity. The portions of the vortex aligned along the rotation axis appear to remain stable somewhat longer. By time $t = 0.8T_\Omega$, we see that small-scale three-dimensional motions have engulfed all portions of the vortex. It is also interesting to note that by this time some cyclonic vorticity begins to align in thin tubes along the ambient rotation axis. By time $t = 1.6T_\Omega$, the peak amplitudes of the vorticity field have

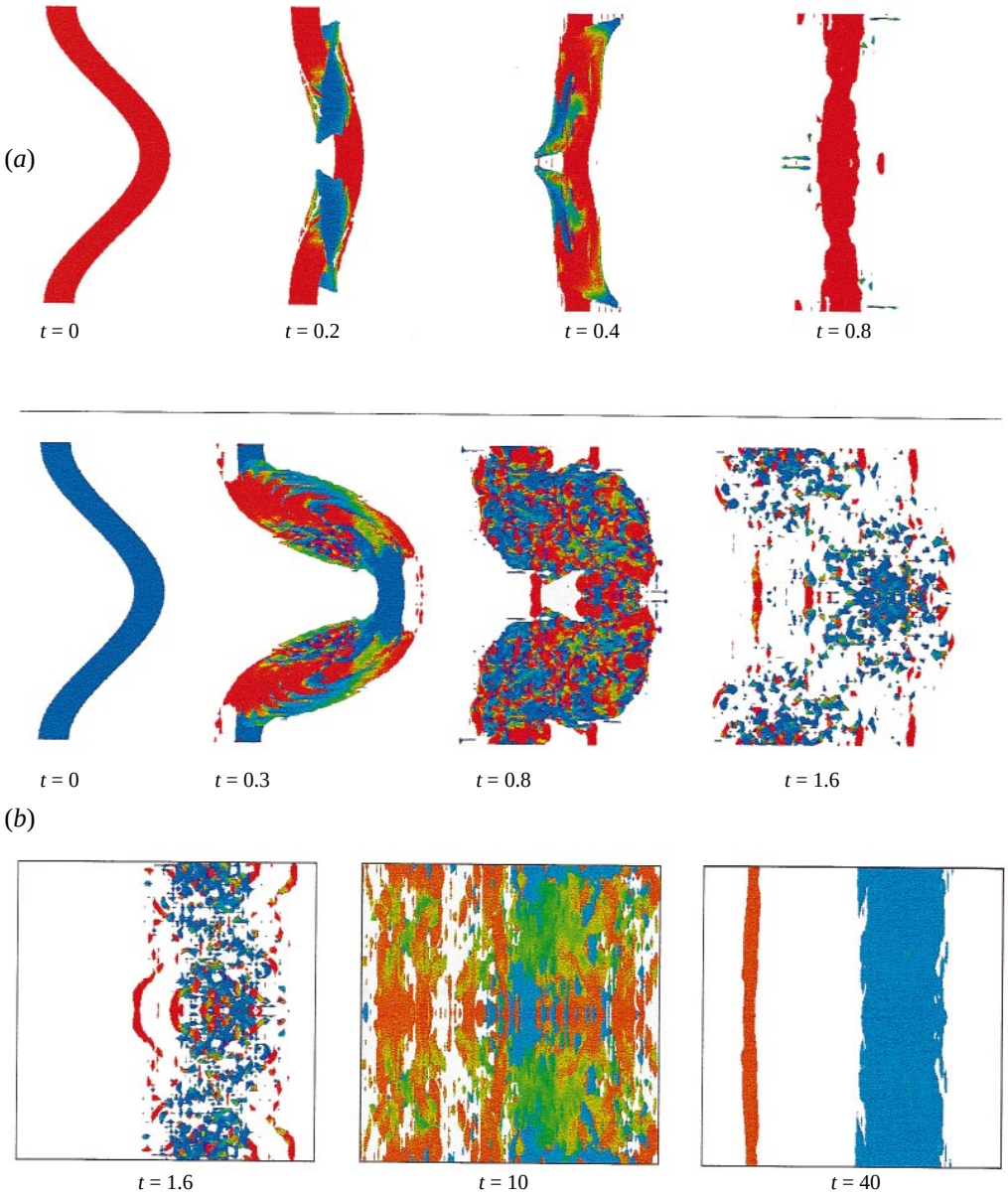

FIGURE 18. The evolution of the strongly perturbed high-Rossby-number (*a*) cyclone and (*b*) anticyclone. (*a*) Evolution of the isosurface $|\omega| = 0.43\boldsymbol{\omega}_0$ for a strongly perturbed cyclone with $Ro = 5$. (*b*) Isosurfaces of $|\boldsymbol{\omega}|$ for a strongly perturbed anticyclone with $Ro = 5$. The isosurface value is $0.43|\boldsymbol{\omega}_0|$ for $t \leqslant 1.6$ and $0.1|\boldsymbol{\omega}_0|$ subsequently. The isosurfaces are coloured according to the value of the vertical vorticity, ω_z, on the isosurface, with a spectrum of colours running from red to blue (red/blue for positive/negative values with green for values near 0). Time is measured in units of the rotation period, T_Ω.

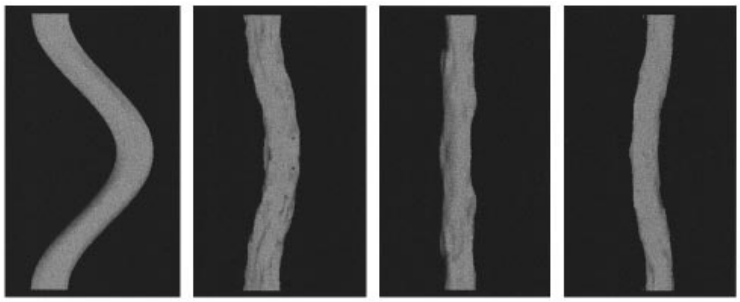

FIGURE 19. Greyscale plot of the $|\omega| = 0.25\omega_0$ isosurface. This plot illustrates the long-term nonlinear evolution of the strongly perturbed cyclone with $Ro = 5$. Times are in units of T_Ω. 'Directional lighting' is used to highlight the three-dimensionality of the structure.

decayed to the point that the isosurface is broken up into small fragments. In the first four plots, the orientation is chosen to show the maximum displacement of the vortex away from the z-axis. The lower three frames (with borders) are viewed along the x-axis just as in the case of the plot showing the initial condition. By time $t = 10T_\Omega$, the peak amplitudes of vorticity are less than $0.2\omega_0$, corresponding to a reduction of the Rossby number based on these amplitudes below $Ro = 1$. Also by this time the entire domain is filled by small-scale three-dimensional motions, although there is a clear tendency toward organization of the vorticity into structures aligned along the ambient rotation direction. As time proceeds, the tendency toward alignment is joined by a tendency toward coalescence of like-signed vorticity. The end result is two tubes, one cyclone and one anticyclone aligned approximately along the axis of ambient rotation. Based on the peak vorticity amplitudes in the centres of these vortices, the Rossby number of the cyclone is about 0.7, while that of the anticyclone is about 0.8, which is in the centrifugally stable range $Ro < 1$. The anticyclone is much broader than the cyclone. It should be pointed out that the perturbation at $t = 0$ was such that at the top and the bottom the tube axis was not displaced. The maximum displacement occurred in the centre ($z = 0$). The final anticyclone shown at $t = 40T_\Omega$ has its axis midway between the extreme horizontal positions of the perturbed vortex at $t = 0$. Thus, in the last graph the axis lies to the right of that of the unperturbed vortex tube.

We have followed the evolution until time $t = 100T_\Omega$. There is some persistence of the bending of the tubes that is evident at time $t = 40T_\Omega$, although this does tend to diminish somewhat. This same numerical experiment has also been performed at resolution 128^3. The results are essentially the same, except that at this higher resolution more thin cyclones are observed to emerge from the turbulent stage shown at time $t = 10T_\Omega$. In figure 20, we show a greyscale isosurface plot of the result of the numerical experiment at resolution 128^3 at time $t = 40T_\Omega$. Here we see that at higher resolution the k_z mode 1 or bending mode is less evident on the anticyclone (thick vortex), and there are three cyclones remaining in the field. At this stage the flow is on the large scales primarily two-dimensional. Therefore, guided by two-dimensional studies (cf. Carnevale *et al.* 1991, 1992), we anticipate that the three cyclones will eventually merge into a single cyclone as in the 64^3 case. Regarding the evolution of the total energy, total enstrophy, and the energy spectrum, the results are very similar to those in the small-perturbation $Ro = 5$ anticyclone case shown in figures 7 and 8. The main difference for the enstrophy evolution is that the peak enstrophy

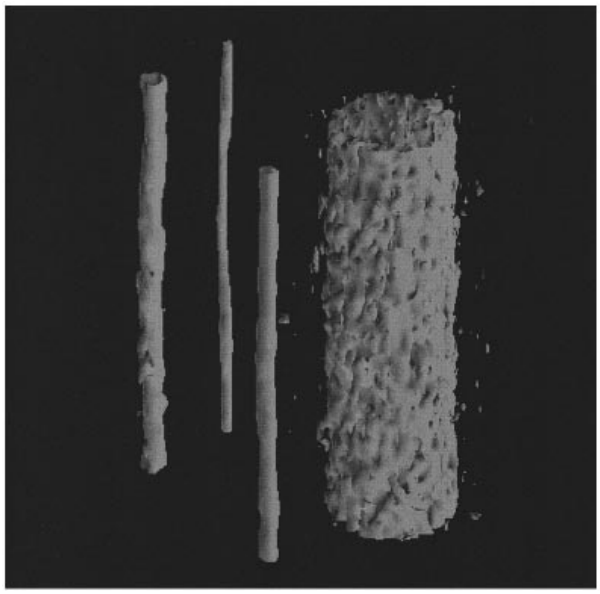

FIGURE 20. Greyscale plot of the $|\omega|$ isosurface for a late stage in the nonlinear evolution of the strongly perturbed anticyclone with $Ro = 5$ from a simulation of resolution 128^3. The isosurface value plotted is $|\omega| = 0.1\omega_0$ at $t = 40T_\Omega$ (to be compared with the corresponding plot in figure 18*b* from a simulation of lower resolution). The thickest tube is an anticyclone, and the three thin tubes are cyclones. 'Directional lighting' is used to highlight the three-dimensionality of the structure.

now occurs at $t = 0.8T_\Omega$. Correspondingly, the fastest energy decay occurs within the first rotation period. The energy spectrum maintains a broad $k^{-5/3}$ range even at late times such as $t = 40T_\Omega$ which is the time of the state shown in figure 20.

8. Summary and discussion

Our purpose in this paper has been to develop some insight into the process whereby a three-dimensional flow may, in the presence of background rotation, become two-dimensional. The Taylor–Proudman theorem cannot explain such two-dimensionalization, since tendencies (time derivatives) are specifically excluded in its derivation. Rather than try to examine the two-dimensionalization problem in the most general context, we focus attention on the dynamics of a vortex column – because it is a tractable problem, offering some hope of providing insight, and because there are associated laboratory experiments. Specifically, we have illustrated, by way of numerical integration, the various effects that a three-dimensional perturbation will have on a Gaussian vortex column aligned along the direction of ambient rotation.

Since the data presented here cover a wide variety of circumstances, it is worthwhile highlighting some of the results before proceeding to final comments. The areas explored can be broken into four classes depending on whether the Rossby number is greater or less than 1 and on whether the perturbation is smaller or larger than the size of the core of the vortex. We will review the most important findings in each category.

8.1. *Small perturbation, small Rossby number*

For very small Rossby numbers (e.g. $Ro = 0.1$), there is very little difference between the evolution of weakly perturbed cyclones and anticyclones. Both relax smoothly toward an axisymmetric state, and the evolution is well represented by linear inertial wave dynamics. This is consistent with (but not explained by) quasi-geostrophic dynamics, valid only in the small Rossby number limit and for which the sign of the vorticity is dynamically irrelevant. For Rossby numbers 0.5 and greater, there are significant differences in the evolution of even weakly perturbed cyclones and anticyclones. At $Ro = 0.5$, although these vortices remain nearly columnar during the evolution, they do not relax to an axisymmetric state like the linear dynamics predicts, but rather they exhibit continuing oscillation of the structure of the column. The amplitudes of both kinds of vortices show moderate decay in time, and although both are stable according to the Rayleigh criterion, the anticyclone decays more rapidly and is more distorted in the long run than the cyclone. For the same period of evolution, a weakly disturbed vortex in the non-rotating environment shows continued increase of small-scale distortions and no tendency toward axisymmetrization on the large scale.

8.2. *Small perturbation, large Rossby number*

For Rossby number greater than 1, the cyclone is centrifugally stable, the anticyclone centrifugally unstable. The tube in the non-rotating environment (infinite Rossby number) is centrifugally stable. For weak perturbations and large (but finite) Rossby number (e.g. $Ro = 5$), the cyclone diminishes somewhat in amplitude during the evolution, but remains close to a Taylor column, although with some small-scale variability imposed on it (see figure 5). The isotropic energy spectrum of the cyclone remains dominated by the large scales with only a low-amplitude flat spectrum for the small scales. The anticyclone exhibits the effect of a rapid centrifugal instability by breaking down into small-scale nearly isotropic turbulence in a time of a few rotation periods. The degree of isotropy was determined by looking at the ratio of enstrophy contributed by ω_z to the total enstrophy, conditioned on the amplitude of the vorticity field (see figure 11). Remarkably, after breakdown, for moderately large Rossby numbers ($1 < Ro \lesssim 25$) the turbulent field reorganizes and a centrifugally stable anticyclone (with $Ro \lesssim 1$) re-emerges (figure 6*d*). This asymptotic anticyclone has a small-scale structure with an isotropic $k^{-5/3}$ energy spectrum superimposed on the large-scale columnar structure. For Rossby numbers greater than about 25, the centrifugal instability is followed by the emergence of both a cyclone and anticyclone, with the cyclone becoming dominant as Ro is increased. The cyclone can stabilize at Ro greater than 1, while the final anticyclone is always such that its Rossby number is less than 1. In the highest Rossby number case tested, the breakdown of a $Ro = 78$ anticyclone, the final state is dominated by a cyclone with a less-coherent anticyclonic vorticity background.

Thus, in the long run, even for flows that are initially centrifugally unstable, the rotating flow is dominated by columnar vortices aligned along the rotation axis. We can wonder how, as Ro is increased, the transition is made from this kind of long-term evolution to that of isotropic turbulence when $Ro = \infty$. For the cyclone, one can imagine that, as the Rossby number is made ever larger, the cyclones would become lost to the superimposed small-scale perturbations, and the degree of anisotropy would diminish. For the anticyclones, as Ro increases, the region of instability, which is beyond radius $r \sim \ln Ro$, moves out well beyond the core of the vortex, and

one can imagine that the rate of return to anisotropy decreases and the degree of two-dimensionalization of the final state will diminish. In this way, there may be a smooth transition to the kind of turbulent breakdown of the vortex at $Ro = \infty$. To a certain extent this scenario for the anticyclones is supported by the graph of Q_z/Q in figure 13. Compared to the $Ro = 5$ case, for the $Ro = 78$ anticyclone the return to anisotropy is delayed, and the degree of anisotropy achieved asymptotically is less.

8.3. *Large perturbation, small Rossby number*

Unlike the case with a weak perturbation, the cyclone with $Ro = 0.5$, when exposed to a large perturbation, goes through a complicated sequence of events (see figures 15 and 16). The tube starts to twist in a complicated fashion, creating anti-parallel vorticity in the early stages. Comparison with the linear dynamics revealed that this stage is describable by linear dynamics, i.e. inertial wave radiation. Soon, nonlinear effects become important, and two tubes of cyclonic vorticity form and merge, forming an elongated tube in the vertical which then relaxes to a horizontally isotropic state on the large scale, but with a strong component of small-scale motions superimposed on it. Nonlinear effects (i.e. the merging of like-signed vorticity) are important as a comparison with the linear dynamics at later times showed (figure 17). In the linear dynamics, the evolution is such that the vorticity field remains highly anisotropic both in the vertical and in the horizontal.

In the experiments of Hopfinger *et al.* (1982) there were many tubes in the tank nearly aligned along the rotation axis, and when these tubes broke down, this could in some instances be attributed to interactions with other vortices. However, in other cases, they speculated that the breakdown had to do with the propagation of soliton-like waves on the tubes. It is interesting to consider the possibility that the breakdown of cyclones that we observed under strong perturbation may be related to the breakdown of the cyclones in their experiment.

For the anticyclone under these conditions of large perturbation but small Rossby number, the scenario is qualitatively the same as that for the cyclone.

8.4. *Large perturbation, large Rossby number*

For the strongly perturbed cyclone of large Rossby number, the motion begins with a decrease in the size of the bend. Then the same linear dynamics which produced the loops in the small Rossby number case begin to produce anti-parallel vorticity as in that case, but here nonlinear processes quickly dominate and no loops are formed (see figure 18*a*). The tube does not break up into two separate tubes, but essentially remains whole and remains much more concentrated than in the small Rossby number case discussed above. The long-term evolution shows that the tube continues to oscillate with a strong bending mode perturbation (see figure 19).

The evolution of the centrifugally unstable anticyclone begins with an increase in the bend or deviation from the rotation axis. Then the vortex breaks down into a highly turbulent field as is shown in figure 18(*b*). The instability is similar to the weakly perturbed case, except that here in the long run, in addition to the establishment of an anticyclonic tube, one or more cyclonic tubes emerge from the turbulent field (depending on the resolution used in the numerical simulations). In the simulation with resolution 64^3, the final separation of the centres of the cyclone and anticyclone is $\sqrt{2}/2$ times the length of one side of the computational domain (see figure 18*b*). Considering the two-dimensional cross-section of the flow taken perpendicular to the ambient rotation direction, this is geometrically the maximum possible separation distance for the two vortices. Thus for two anti-parallel vortices, this is the maximum

energy configuration (cf. Carnevale & Vallis 1990). Perhaps there is some connection here with the process of selective decay (cf. Matthaeus *et al.* 1991) in the sense that there may be a tendency to decay certain vortical invariants on a time scale faster than the energy decay. However the end state here is far from that predicted by selective decay (cf. Carnevale *et al.* 1991, 1992 and Matthaeus *et al.* 1991).

8.5. *Final remarks*

There appears to be no simple or general answer as to how rotation mediates the tendency towards Taylor-column formation in the case of single tubes exposed to non-axisymmetric perturbations. Only for small Rossby numbers and small perturbations can one say that it is simply due to radiation of inertial waves. For small Rossby numbers and large perturbations, only the early stages of the evolution is governed linear dynamics, but nonlinear effects like merger of like-signed vorticity help to establish vertically invariant flows which are on average circularly symmetric in the horizontal plane. The word 'help' is appropriate here because the experiments without background rotation showed that without rotation the centrifugally stable tubes exposed to non-axisymmetric perturbations always break down into a turbulent field without a return to anisotropy.

In addition to the interplay between linear and nonlinear effects, viscous effects can also play an important role in two-dimensionalization. Here we have only included eddy viscous effects with the sole purpose of allowing the nonlinear cascade of energy to high wavenumber to proceed. In laboratory experiments in rotating tanks where two-dimensionalization is apparent, vorticity diffusion due to molecular viscosity also plays a role, particularly through the establishment of an Ekman boundary layer at the bottom of the tank and boundary layers on the vertical sidewalls. These boundary layers can absorb inertial wave radiation from the evolving vortex (Greenspan 1968), thus aiding the two-dimensionalization of the vortex. A more complete investigation of viscous effects is a topic of future study.

In geophysical flows, density stratification also plays an important role in the evolution of vortex columns. In the quasi-geostrophic approximate dynamics, which incorporates both rotation and stratification, McWilliams, Weiss, & Yavneh (1994) showed that a three-dimensional isotropic small-scale randomly generated vorticity field evolves toward a state of vortex columns aligned along the rotation axis. It would be interesting to explore the roles that rotation and stratification each play in this phenomenon in three-dimensional simulations without invoking the quasi-geostrophic approximation. Vallis, Shutts & Gray (1996) have performed some preliminary simulations in this regard, but the subject is still largely unexplored.

This research has been supported in part by Office of Naval Research grants N00014-97-1-0095, N00015-96-1-0065 and N00014-96-1-0452, and by National Science Foundation grants OCE 91-21998, ATM 93-9317485, and INT-9511552. The numerical simulations were performed at IBM-ECSEC, European Center for Scientific & Engineering Computing, at CINECA using the IBM SP2, and at the San Diego Super Computer Center.

REFERENCES

Bardina, J., Ferziger, J. H. & Rogallo, R. S. 1985 Effect of rotation on isotropic turbulence: computation and modelling. *J. Fluid Mech.* **154**, 321–336.

Bartello, P., Metais, O. & Lesieur, M. 1994 Coherent structures in rotating three-dimensional turbulence. *J. Fluid Mech.* **273**, 1–29.

Batchelor, G. K. 1967 *An Introduction to Fluid Dynamics*. Cambridge University Press.

Briscolini, M. & Santangelo, P. 1992 Numerical simulations of three-dimensional homogeneous isotropic flows. In *Proc. Conf. on Parallel Computing: Problems, Methods and Applications* (ed. P. Messina & A. Murli). Elsevier.

Cambon, C., Benoit, J. P., Shao, L. & Jacquin, L. 1994 Stability analysis and large eddy simulation of rotating turbulence with organized eddies. *J. Fluid Mech.* **278**, 175–200.

Cambon, C. & Jacquin, L. 1989 Spectral approach to non-isotropic turbulence subjected to rotation. *J. Fluid Mech.* **202**, 295–317.

Cambon, C., Jacquin, L. & Lubrano, J. L. 1992 Toward a new Reynolds stress model for rotating turbulent flows. *Phys. Fluids* A **4**, 812–824.

Carnevale, G. F., Cavazza, P., Orlandi, P. & Purini, R. 1991 An explanation for anomalous vortex merger in rotating tank experiments. *Phys. Fluids* A **3**, 1411–1415.

Carnevale G. F. & Kloosterziel R. C. 1994, Emergence and evolution of triangular vortices. *J. Fluid Mech.* **259**, 305–331.

Carnevale, G. F., Kloosterziel, R. C. & Heijst, G. J. F. van 1991 Propagation of barotropic vortices over topography in a rotating tank. *J. Fluid Mech.* **233**, 119–139.

Carnevale, G. F., McWilliams, J. C., Pomeau, Y., Weiss, J. B. & Young, W. R. 1991 Evolution of vortex statistics in two-dimensional turbulence. *Phys. Rev. Lett.* **66**, 2735–2737.

Carnevale, G. F., McWilliams, J. C., Pomeau, Y., Weiss, J. B., & Young, W. R. 1992 Rates, pathways, and end states of nonlinear evolution in decaying two-dimensional turbulence: scaling theory versus selective decay. *Phys. Fluids* A **4**, 314–316.

Carnevale, G. F. & Shepherd, T. G. 1990 On the interpretation of Andrew's theorem. *Geophys. Astrophys. Fluid Dyn.* **51**, 1–17.

Carnevale, G. F. & Vallis, G. K. 1990 Pseudo-advective relaxation to stable states of inviscid two-dimensional fluids. *J. Fluid Mech.* **213**, 549–571.

Carton, X. & Legras, B. 1994 The life-cycle of tripoles in two-dimensional incompressible flow. *J. Fluid Mech.* **267**, 53–82.

Chandrasekhar, S. 1961 *Hydrodynamic and Hydromagnetic Stability*. Oxford University Press.

Chollet, J. P. & Lesieur, M. 1981 Parameterization of small scales of three-dimensional isotropic turbulence utilizing spectral closure. *J. Atmos. Sci.* **38**, 2747–2757.

Dritschel, D. G. 1988 Nonlinear stability bounds for inviscid, two-dimensional, parallel or circular flows with monotonic vorticity, and the analogous three-dimensional quasi-geostrophic flows. *J. Fluid Mech.* **191**, 575–581.

Flierl, G. R., Stern, M. E. & Whitehead, J. A. 1983 The physical significance of modons: laboratory experiments and general integral constraints. *Dyn. Atmos. Oceans* **7**, 233–263.

Grant, H. L., Stewart, R. W. & Moilliet A. 1962 Turbulence spectra from a tidal channel. *J. Fluid Mech.* **12**, 241-263.

Greenspan, H. P. 1968 *The Theory of Rotating Fluids*. Cambridge University Press.

Heijst, G. J. F. van, Kloosterziel, R. C. & Williams, C. W. M. 1991 Laboratory experiments on the tripolar vortex in a rotating fluid. *J. Fluid Mech.* **225**, 301–331.

Hopfinger, E. J., Browand, F. K. & Gagne, Y. 1982 Turbulence and waves in a rotating tank. *J. Fluid Mech.* **125**, 505–534.

Jacquin, L., Leuchter, O., Cambon, C. & Mathieu, J. 1990 Homogeneous turbulence in the presence of rotation. *J. Fluid Mech.* **220**, 1–52.

Kelvin, Lord 1880 Vibrations of a columnar vortex. *Phil. Mag.* **10**, 155–168.

Kloosterziel, R. C. & Heijst, G. J. F. 1991 An experimental study of unstable barotropic vortices in a rotating fluid. *J. Fluid Mech.* **223**, 1–24.

Kraichnan, R. H. 1976 Eddy viscosity in two and three dimensions. *J. Atmos. Sci.* **33**, 1521–1536.

Lesieur, M. & Rogallo, R. 1989 Large-eddy simulation of passive scalar diffusion in isotropic turbulence. *Phys. Fluids* A **1**, 718–722.

Lesieur, M., Yanase, S. & Metais, O. 1991 Stabilizing and destabilizing effects of a solid-body rotation on quasi-2-dimensional shear layers. *Phys. Fluids* A **3**, 403–407.

Leslie, D. C. 1973 *Developments in the Theory of Turbulence*. Clarendon Press.

Lighthill, M. J. 1978 *Waves in Fluids*. Cambridge University Press.

Lundgren, T. S. & Ashurst, W. T. 1989 Area-varying waves on curved vortex tubes with application to vortex breakdown. *J. Fluid Mech.* **200**, 283–307.

Mahalov, A. & Zhou, Y. 1996 Analytical and phenomenological studies of rotating turbulence. *Phys. Fluids* **8**, 2138–2152.

Matthaeus, W. H., Stribling, W. T., Martinez, D., Oughton, S. & Montgomery, D. 1991 Selective decay and coherent vortices in two-dimensional incompressible turbulence. *Phys. Rev. Lett*. **66**, 2731–2734.

McWilliams, J. C., Weiss, J. B. & Yavneh, I. 1994 Anisotropy and coherent vortex structures in planetary turbulence. *Science* **264**, 410–413.

Melander, M. V. & Hussain, F. 1989 Cross-linking of two antiparallel vortex tubes. *Phys. Fluids* A, **1**, 633–636.

Melander, M. V., McWilliams, J. C. & Zabusky, N. J. 1987 Axisymmetrization and vorticity-gradient intensification of an isolated two-dimensional vortex through filamentation. *J. Fluid Mech.* **178**, 137–159.

Melander, M. V., Zabusky, N. J. & McWilliams, J. C. 1988 Symmetric vortex merger in two dimensions: causes and conditions. *J. Fluid Mech.* **195**, 303–340.

Miyazaki, T. & Fukomoto, Y. 1991 Axisymmetric waves on a vertical vortex in a stratified fluid. *Phys. Fluids* A **3**, 606–616.

Patterson, G. S. & Orszag, S. A. 1971. Spectral calculations of isotropic turbulence, efficient removal of aliasing interactions. *Phys. Fluids* **14**, 2538–2541.

Rayleigh, Lord 1916. On the dynamics of revolving fluids. *Proc. R. Soc. Lond.* A **93**, 148–154.

Saffman, P. G. 1992 *Vortex Dynamics*. Cambridge University Press.

Smyth, W. D. & Peltier, W. R. 1994 Three-dimensionalization of barotropic vortices on the *f*-plane. *J. Fluid Mech.* **265**, 25–64.

Vallis, G. K., Shutts, G. J. & Gray, M. E. B. 1996 Balanced mesoscale motion and stratified turbulence forced by convection. Submitted to *Q. J. R. Met. Soc.*

Vincent, A. & Meneguzzi, M. 1991 The spatial structure and statistical properties of homogeneous turbulence. *J. Fluid Mech.* **225**, 1–20.